A Computational Framework to Study Neural-Structural Interactions in Human Walking

by

Pavitra Krishnaswamy

B.S., Electrical Engineering and B.S., Physics
University of Southern California (2003)

Submitted to the Department of Electrical Engineering and Computer Science
in partial fulfillment of the requirements for the degree of

Master of Science in Electrical Engineering

at the

MASSACHUSETTS INSTITUTE OF TECHNOLOGY

February 2010

Author .....
Department of Electrical Engineering and Computer Science
Dec 15, 2009

Certified by .....
Hugh Herr
Associate Professor of Health Sciences and Technology
Associate Professor of Media Arts and Sciences
Thesis Supervisor

Certified by .....
Emery N. Brown
Professor of Health Sciences and Technology
Professor of Computational Neuroscience
Thesis Supervisor

Accepted by .....
Terry P. Orlando
Chair, Department Committee on Graduate Students

A Computational Framework to Study Neural-Structural Interactions in Human Walking

by
Pavitra Krishnaswamy

Submitted to the Department of Electrical Engineering and Computer Science
on Dec 15, 2009, in partial fulfillment of the
requirements for the degree of
Master of Science in Electrical Engineering

Abstract

Neuroscientists researching locomotion take a top-down approach by elucidating high-level cortical control circuits. In contrast, biomechanists prefer to focus on structural and mechanical aspects of the legged movement apparatus. We posit that studying interplay between neural co-ordination and legged biomechanics can yield crucial insight into (a) motor control and (b) human leg morphology. Physiological facts indicate that muscle actuator state (activation, length and velocity) is key to this neural-structural interplay. Here we present a novel model-based framework to resolve individual muscle state and describe neural-structural interactions in normal gait.

We solve the inverse problem of using kinematic, kinetic and electro-myographic data recorded on healthy humans during level-ground,self-selected speed walking to estimate state of three major ankle muscles. Our approach comprises of two steps. First, we estimate neurally-controlled muscle activity from EMG data by building on statistical and mechanistic methods in the literature. Second, we perform a system ID on a mechanistic (Hill-type) model of the three muscles to find tendon morphological parameters governing evolution of muscle length and velocity. We implement the parameter identification as an optimization based on the hypothesis that neural control and lower limb morphology have co-evolved for optimal metabolic economy of natural walking. We cross-validate our framework against independent datasets, and find good model-empirical ankle torque agreement ($R^2 = 0.96$).

The resulting muscle length and velocity predictions are consistent with *in vivo* ultrasound scan measures. Further, model predictions reveal how leg structure and neural control come together to (a) define roles of individual plantar flexor muscles and (b) boost their joint performance. We find that the Soleus operates as a steady efficient force source, while the Gastrocnemius functions as a burst mechanical power source. An analysis of the estimated states and optimized parameters reveals that the plantar flexors operate jointly at a net mechanical efficiency of 0.69 ± 0.12. This is roughly three times higher than the maximal efficiency of skeletal muscle performing positive work. Our results suggest that neural control may be tuned to exploit the elasticity of tendinous structures in the leg and achieve the high walking economy of humans.

Thesis Supervisor: Hugh Herr
Title: Associate Professor of Health Sciences and Technology
Associate Professor of Media Arts and Sciences

Thesis Supervisor: Emery N. Brown
Title: Professor of Health Sciences and Technology
Professor of Computational Neuroscience

Acknowledgments

There are many people who have supported me through the process leading to this thesis. I would like to express my sincere thanks to:

Both my thesis supervisors for coming together to advise me on this project. Hugh Herr for his insightful guidance, and for teaching me to think mechanistically about modeling physiology. Emery Brown for giving me the intellectual freedom to develop and pursue research problems of interest to me, and for teaching me to approach statistical techniques with biophysical intuition.

My collaborators for their help, advice and time. Eric Swart and Todd Farrell for help with experiments - Eric for spending many hours and sharing his expertise in data collection, Todd for his help with the software and camera system; Hartmut Geyer for providing me the base implementation of the Hill muscle model; Ken Endo for sharing his work on walking models, and for introducing me to the developing world applications of our work; Michael Eilenberg for the many hours of whiteboard discussions, and help in developing the Achilles tendon argument in Chapter 5; Zhe Chen for the lunch meetings and discussions on EMG analysis; Peter Loan for his patience and kindness in helping me process data in SIMM; Jing Wang for her help in processing data at odd hours of night, and for her infectious enthusiasm to learn and contribute; Iahn Cajigas for exposing me to the clinical side, and sharing resources and feedback.

The subjects who were kind enough to get instrumented, walk at my command for many hours, and give me their data.

To all the people I work with for the fellowship, enriching discussions and for making work fun. Bruce Deffenbaugh for teaching me to break down complex problems, dinner and dessert outings, long distance phone consultations and timely doses of reality; Todd Farrell, Michael Eilenberg and Jared Markowitz for lightening up our erstwhile 095 office; Grant Elliott for the many fun physics and puzzle solving discussions; Ernesto Martinez for making late-night working enjoyable; Diana Young and Alena Grabowski for being inspiring post-docs; and Sarah Hunter for facilitating work and life on a daily basis. All of you made everyday very memorable.

My academic advisor, Prof. Martha Gray, for helping me navigate the challenges of graduate school.

My roommates and friends for keeping me sane and cheerful - the former for wine and late night porch discussions; the latter for helping me have a life outside of work.

Anjan Soumyanarayanan for being the most wonderful partner I could wish for. I am grateful to have you in my life.

My parents Mr. N. Krishnaswamy and Mrs. Mala Krishnaswamy: I am forever indebted to your love, unwavering support, generosity and commitment to my well-being. I dedicate this thesis to both of you.

Contents

1 Introduction **15**
- 1.1 Context . . . 16
- 1.2 Literature Survey . . . 16
  - 1.2.1 Inverse Modeling . . . 16
  - 1.2.2 Forward Modeling . . . 17
- 1.3 Thesis Objectives . . . 18
- 1.4 Chapter Summary . . . 18

2 Background **21**
- 2.1 Walking . . . 21
  - 2.1.1 Gait Cycle . . . 21
  - 2.1.2 Locomotion Energetics . . . 22
- 2.2 Muscle-Tendon Units of Ankle-Foot Complex . . . 22
- 2.3 Muscle Physiology . . . 24
  - 2.3.1 Structure . . . 24
  - 2.3.2 Force Generation . . . 24
  - 2.3.3 States and Dynamics . . . 25
  - 2.3.4 The Hill-type Muscle Model . . . 25
- 2.4 Tendon Physiology . . . 26
- 2.5 Neural-Structural Interactions . . . 26
- 2.6 Problem Statement . . . 27

3 Methods **29**
- 3.1 Data Collection Procedures . . . 29
- 3.2 Data Processing . . . 31
  - 3.2.1 Joint State . . . 31
  - 3.2.2 Muscle-Tendon State . . . 32
- 3.3 Estimation of Muscle State . . . 33
- 3.4 Neural Control to Individual Muscles . . . 34
  - 3.4.1 Biophysics of Muscle Activation . . . 34
  - 3.4.2 Estimation of Muscle Activation . . . 36
  - 3.4.3 Implementation Algorithm . . . 38
  - 3.4.4 Results . . . 39
  - 3.4.5 Active State Estimation Summary . . . 40
- 3.5 Influence of Tendon Morphology on Muscle Action . . . 41

3.5.1 System ID Problem . . . 41
3.5.2 System Model . . . 41
3.5.3 Inputs to Muscle-Tendon Model . . . 45
3.5.4 Parameter ID Problem . . . 46
3.5.5 Implementing Optimization . . . 50
3.5.6 Optimization Results . . . 52
3.5.7 System ID Summary . . . 55
3.6 Chapter Summary . . . 55

4 Efficacy of Approach **57**
4.1 EMG-Activation Estimation Technique . . . 57
4.1.1 Robustness . . . 57
4.1.2 Limitations . . . 58
4.1.3 Future Work . . . 59
4.2 System-ID Procedure . . . 60
4.2.1 Speed Invariance . . . 60
4.2.2 Uniqueness of Optimizer Solution . . . 61
4.3 Cross-Validation . . . 64
4.4 Chapter Summary . . . 66

5 Results and Discussion **67**
5.1 Muscle Length and Velocity . . . 67
5.1.1 Length . . . 68
5.1.2 Velocity . . . 72
5.1.3 Section Summary . . . 74
5.2 Roles of Soleus and Gastrocnemius Muscles . . . 74
5.2.1 Structure . . . 74
5.2.2 Control . . . 75
5.2.3 Structure and Control . . . 75
5.2.4 Section Summary . . . 76
5.3 Ankle Plantar Flexor Performance . . . 76
5.3.1 Structure - Conserved Morphological Features . . . 76
5.3.2 Control - Timing Elastic Storage and Release . . . 78
5.3.3 Structure and Control: Efficiency . . . 79
5.3.4 Section Summary . . . 81
5.4 Discussion . . . 82
5.4.1 Dynamic Optimization Studies . . . 82
5.4.2 Simple Mechanistic Muscle-Tendon Models . . . 82
5.4.3 Section Summary . . . 83
5.5 Chapter Summary . . . 83

6 Conclusions and Future Work **85**
6.1 Conclusions . . . 85
6.2 Scientific Applications . . . 85
6.3 Engineering Applications . . . 87

List of Figures

1-1 Hierarchy of Systems involved in Locomotion 15

2-1 Gait Cycle Phase Divisions 22
2-2 Muscles and Tendons of the Ankle-Foot Complex 23
2-3 Placing neural control, muscle actuation, tendon transmission and environmental perception in the hierarchical context 27

3-1 Ankle angles and moments for 5 subjects 32
3-2 Muscle-tendon unit length and moment arms for 5 subjects 33
3-3 Biophysics of muscle activation 35
3-4 From raw EMG data to muscle activation estimate 39
3-5 Activation estimates for 3 ankle muscles for 5 subjects 40
3-6 Modeled ankle muscle-tendon units 42
3-7 Empirically based muscle metabolic power as a function of velocity . 48
3-8 Convergence of the constrained genetic algorithm optimization 53
3-9 Model-empirical ankle torque agreement after training 53
3-10 Summary of approach - from motion capture data to muscle states . . 56

4-1 Robustness of muscle activation estimation 58
4-2 Limitation of activation estimation algorithm 59
4-3 Repeatability of Soleus tendon stiffness 62
4-4 Training versus testing inputs to model 64
4-5 Agreement of ankle torque from independently trained model with test data 65

5-1 Model estimates of Soleus muscle length 68
5-2 *In vivo* measure of Soleus muscle length 68
5-3 Model estimate of Gastrocnemius muscle length 70
5-4 *In vivo* measure of Gastrocnemius muscle length 70
5-5 Model estimates of Gastrocnemius length for a second subject 71
5-6 A second *in vivo* measure of Gastrocnemius length 71
5-7 Model estimates of Soleus muscle velocity 73
5-8 Model estimates of Gastrocnemius muscle velocity 73

List of Tables

3.1 Subjects for Motion Capture Data Collection 30
3.2 Parameters defining Hill muscle model equations 43
3.3 Parameters defining muscle-tendon dynamics 45
3.4 Optimization Bounds for Tendon Morphological Parameters 50
3.5 Genetic Algorithm Optimization Settings 51
3.6 Optimization Results 54

4.1 Invariance of Morphological Parameters Across Speed 60
4.2 Uniqueness of Solution: Soleus Tendon Parameter Trends 61
4.3 Uniqueness of Solution: Other Muscle-Tendon Units? 63
4.4 Uniqueness of Solution - Achilles Tendon Parameter Trends 63
4.5 Cross-Validation of Model 65

5.1 Plantar Flexor Ankle Moment Breakdown 75
5.2 Stiffness of Different Tendons in the Model 77
5.3 Muscle Rest Length to Tendon Slack Length Ratios 78
5.4 Plantar Flexor Positive Work Efficiency (No Tendon) 79
5.5 Plantar Flexor Net Mechanical Efficiency (With Tendon) 81

1 Subject-Specific (Scaled) Muscle-Tendon Parameters 89
2 Subject-Specific Optimization Bounds 90

List of Terms

Afferent: Afferent neurons carry nervous impulses from peripheral receptors and sense organs toward the central nervous system.

Efferent: Efferent neurons carry nervous impulses away from the central nervous system to effectors such as muscles.

Muscle-Tendon Unit: The combination of a muscle actuator (muscle) and the tendon connecting the muscle to skeleton. The unit generates force by a combination of a muscle action and storage/release of elastic energy in the tendon. Also referred to as muscle-tendon complex (MTC), musculo-tendon unit (MTU) or musculo-tendon complex.

Morphology: A branch of biology dealing with the form and structure of a living organism and/or its parts

Histology: The study of the microscopic anatomy of living tissues Sagittal Plane: the plane dividing the body into left and right sections

Chapter 1

Introduction

Locomotion is a highly concerted effort coordinated by a multitude of physiological systems. Control commands initiated in the brain travel through the spinal cord and the peripheral nervous system down to skeletal muscles that actuate the lower limbs. The forces generated by muscles are transmitted through the tendinous structures to the skeleton. Forces on the skeleton cause joint motion and mechanical interactions with the environment. These interactions are fed back to the nervous system through the tendons, muscle sensors and visual/proprioceptive circuits. The environmental and sensory information relayed back facilitates maintenance of the rhythmic feature of gait, and also helps in control and planning of next steps. A lumped component description of this system would group the nervous system blocks and the musculo-skeletal structures in the leg as 'neural controller' and 'plant' respectively (Figure 1-1). This thesis is about understanding the interactions between the nervous system (controller) and the leg structures (plant) in human walking.

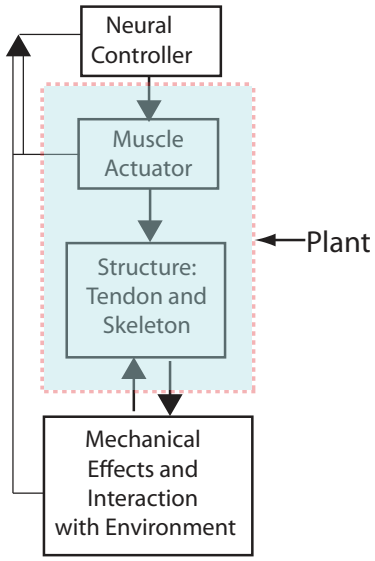

Figure 1-1: Hierarchy in physiological systems influencing locomotion. We refer to the shaded block as the 'Plant'.

1.1 Context

To understand interactions, we need to first place them in context of the mechanical and neural aspects of locomotion.

It has been argued that mechanical aspects dominate human walking. Inverse pendulum walkers and passive dynamical robots, having little control or actuation, largely mimic trends observed in human walking [1, 2]. Logically, this leads to the expectation that changing mechanical loading and speed requirements would cause significant changes in motions. However, there is evidence that kinematic profiles are conserved across walking speed and body weight load [3]. This could be interpreted as the influence of some feed-forward neural encoding of kinematics. The feed-forward hypothesis becomes unlikely if we consider the major kinematic variations between air-stepping and ground-stepping [3]. Thus, it appears that perception and sensation of ground contact are defining factors. This is very reasonable given the rhythmic nature of locomotion - as perception and contact are key to rhythmic phase transitions in many systems [4]. Physically, these phase transitions may be enforced via feedback circuits communicating lower level sensation of contact to higher level neural controller structures, and vice versa. By definition, this interplay has to be mediated via the musculo-skeletal structures in the leg where the neural feedback sensors and muscle actuators are located. Thus, the interplay between neural control and mechanical effects is significant in locomotion, and is mediated by the musculo-skeletal structures in the leg (plant).

1.2 Literature Survey

The study of this interplay is at a level in between the extremes of passive dynamic mechanical models [1] and purely feed-forward pattern generator models [5]. Neural co-ordination at the level of the musculo-skeletal structures in the leg has been studied widely by the neuromuscular modeling community. But the interaction between the neural and mechanical components is not sufficiently captured in existing models which belong to the two categories discussed below.

1.2.1 Inverse Modeling

These studies try to infer features of neural coordination or leg structure from in vivo motion capture studies. Most inverse studies have focused on inferring either of the above.

Inferring Neural Control

To infer neural coordination features, dynamic optimization approaches have been proposed [6, 7]. These studies use physiological models of musculo-skeletal structures in the leg, and dynamically optimize time-varying neural commands that activate different sets of muscles - to track in vivo data and/or minimize some performance-

related cost objectives. There are three main questions relating to the accuracy and uniqueness of the optimized activation estimates.

- Firstly, the actual objectives governing neural activation can be complex and the differences in goals of different muscles may not be captured in the modeled costs.

- Secondly, there is no systematic consideration of the variability in neural commands activating muscles and the redundancy in the neuromuscular system wherein different sets of activation patterns could lead to the same gross mechanical effects.

- Finally, most of these studies set the many parameters governing the plant dynamics (musculo-skeletal models) from values in literature even though there are no standard techniques to capture subject-to-subject variations in these parameters.

Thus, these studies do not appropriately capture the interplay between neural control and leg structure - as they set the leg structure and optimize for the highly variable neural control features based on controversial objective functions.

Inferring Leg Structure

Other inverse studies have focused on capturing the key features of muscle-tendon structure and behavior in locomotion by hypothesizing mechanistic approximations of musculo-skeletal dynamics. In one such study, plant dynamics is represented through clutch-spring approximations [8]. This minimalist representation is based on the hypothesis that muscle-tendon units work like linear springs when they are 'clutched' on by the neural commands activating muscles. These mechanistic models have higher predictive power, elucidate general principles of legged mechanics and tell us that spring-like behavior of muscles may be key to walking. However, they too, do not capture the interplay between neural control and leg structure as they lump both the active neurally controlled muscle and passive structural tendon elements into springs. To capture the interplay, it is important to decouple the active and passive structures.

1.2.2 Forward Modeling

To avoid the computational problems in capturing both key aspects of neural control and leg structure in inverse problems, researchers have built forward models to capture interplay between these two aspects. These models are based on physics-based guesses of controllers that lead to observed trends of legged mechanics in walking. For example, it has been shown that a purely reflex-actuated model capturing the conceptual features of neural-mechanical interaction adapts to terrain variations [9]. While such models have the power to resolve high level features and suggest experiments, it is hard to verify them directly against ground truth. *In vivo* measures of

accuracy of the proposed controllers are often inaccessible. Further, with such forward approaches, it is hard to obtain detailed resolution of control features without resorting to manual tuning or approximations of a multitude of parameters.

In summary, neither the inverse approaches nor the forward approaches existing in the literature fully capture the interactions between neural control and leg structure in locomotion. Thus, it is important to develop a framework that can (a) capture the physics of the interplay like the forward methods and (b) obtain high granularity of information from empirical data without compromising the physics of the interactions we seek to understand.

1.3 Thesis Objectives

The goal of this thesis is to develop a modeling framework that uses human gait data to capture quantitative insights about the interplay between neural and structural aspects governing ankle behavior during walking.

Taking inspiration from biophysical features governing these interactions, we reframe the inverse problem as a two-step combination of (a) a hidden state estimation and (b) system ID problem. We anticipate that each of these steps will address computational difficulties faced by previous efforts, without compromising the important physics involved.

First, we address challenges arising from system redundancy and neural control variability by building on physical and statistical techniques to estimate neural control from in vivo electro-myographic data. Then, we hypothesize that neural control and leg structure have co-evolved for optimal economy of natural walking. We use this hypothesis to drive an optimization and identify key invariant parameters defining actions of musculo-skeletal structures.

We find a model structure that predicts human-like ankle torque from empirically based inputs about ankle motion and muscle activity. Finally, we use this model to probe (a) ankle muscle state profiles, (b) roles of individual ankle muscles, (c) performance metrics regarding function of ankle muscles and (d) structural and neural features governing design and control of the ankle muscles during walking.

1.4 Chapter Summary

In Chapter 2, we introduce several aspects of the physiology and gait biomechanics that would aid in reading this thesis.

In Chapter 3, we detail the computational framework to estimate muscle state from motion capture data. We propose a hybrid statistical-mechanistic estimator of muscle active state from electro-myographic data, and develop a system ID procedure for identifying key morphological parameters needed for estimating muscle length and velocity.

In Chapter 4, we evaluate the effectiveness of the methods from Chapter 3. We discuss robustness and sensitivity issues influencing the muscle activation estimates.

Then we describe analytical experiments performed to validate the system ID approach and understand the solutions. Finally, we cross-validate the entire framework on test datasets.

In Chapter 5, we present model predictions regarding leg structure, neural control and the interplay between the two aspects. We present ankle muscle state estimates, discuss role-division between the two posterior-leg muscles and present several metrics suggestive of their function and energetic performance.

Finally, in Chapter 6, we summarize the conclusions of our study and suggest directions for future work in both the scientific and device engineering realms.

Chapter 2

Background

This chapter introduces concepts and facts relating to biomechanics, musculo-skeletal structures and neural control that may be useful in reading this thesis. We start by introducing general gait analysis facts and terminology. Then, we outline biomechanical and anatomical features affecting human ankle motion in walking. In the last few sections, we delve into the relevant physiology of neural control, muscle actuation, tendon transmission and the interactions between these different aspects. The descriptions are developed from biological, systems and physics viewpoints. We end the chapter with a detailed statement of the problem solved in this thesis.

2.1 Walking

In this section, we introduce some terminology relating to gait analysis and commonly accepted energetic features governing walking.

2.1.1 Gait Cycle

Human walking is a periodic motion, and is often analyzed with reference to normalized time periods - ranging from 0-100% of gait cycle (GC). Consecutive heel-strikes of the same limb designate the start and end of a period (0% and 100% points). Typically, walking is analyzed for data over one gait cycle. Hence all plots of data in this thesis will be presented with respect to gait phase or percent gait cycle units.

Figure 2-1 shows the division of gait cycle into phases. Primary periods of interest for this thesis are the stance-phase (during ground contact) and the swing-phase (when a limb is not in contact with ground). Early stance is used to refer to the initial contact and loading phases, before the contra-lateral foot is lifted off for swing. Pre-swing refers to the final phase of stance between contralateral heel strike and ipsilateral toe-off. Toe-off is used to designate the end of stance phase and the beginning of swing phase for a given leg.

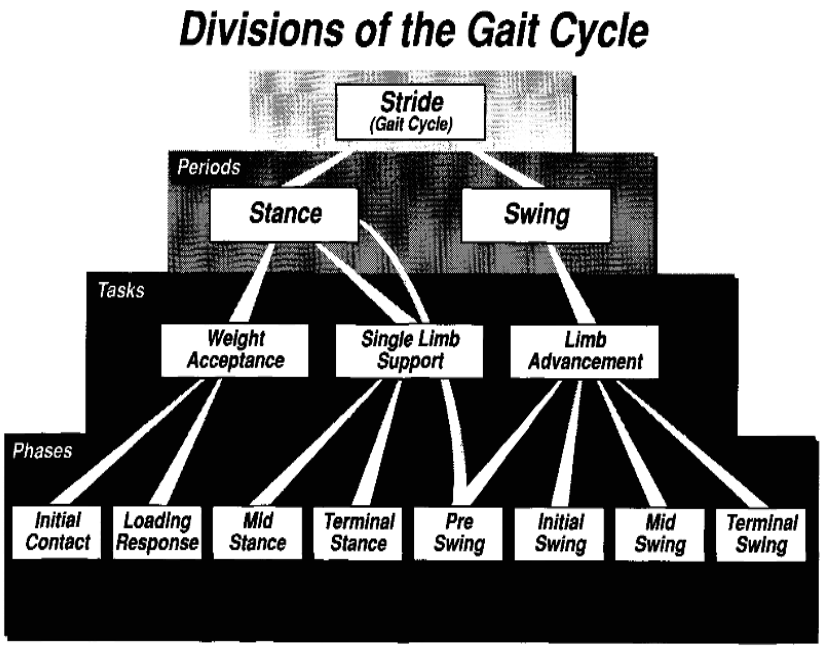

Figure 2-1: Gait Cycle Phase Divisions: Source [10]

2.1.2 Locomotion Energetics

The major sources of energy expenditure during locomotion come from the need to activate muscles and move the body forward/against gravity. Energy cost for most natural walking speeds has a quadratic dependence on speed [11]. There are variations of this quadratic dependence that account for step length and step rate, but they all have the same general monotonically increasing trend with speed. However, a metric commonly used for energy expenditure in locomotion is the energy expended per unit distance walked normalized by subject weight ($J/(kg \cdot m)$). This metric, also referred to as locomotion economy in this thesis, has a concave up relationship with walking speed. As discussed in [11], it has been shown that a person walking in a natural self-selected manner adopts speeds close to the most economic speed. Therefore, for a subject walking at their preferred speed, it is safe to assume that the metabolic energy consumed has to be close to the minimum of the metabolic energy per unit distance traveled. Further, if the motion of the subject is known consistently at self-selected walking speeds, the metabolic energy consumed corresponds to the minimum metabolic energy expenditure for that subject's walking motion.

2.2 Muscle-Tendon Units of Ankle-Foot Complex

Much of the motion involved in level ground walking is in the sagittal plane. In this section we introduce the major structures influencing sagittal plane motion of the

ankle joint we study in this thesis. These include the Triceps Surae muscle-tendon units, the Tibialis Anterior muscle-tendon unit and the Achilles tendon (Figure 2-2).

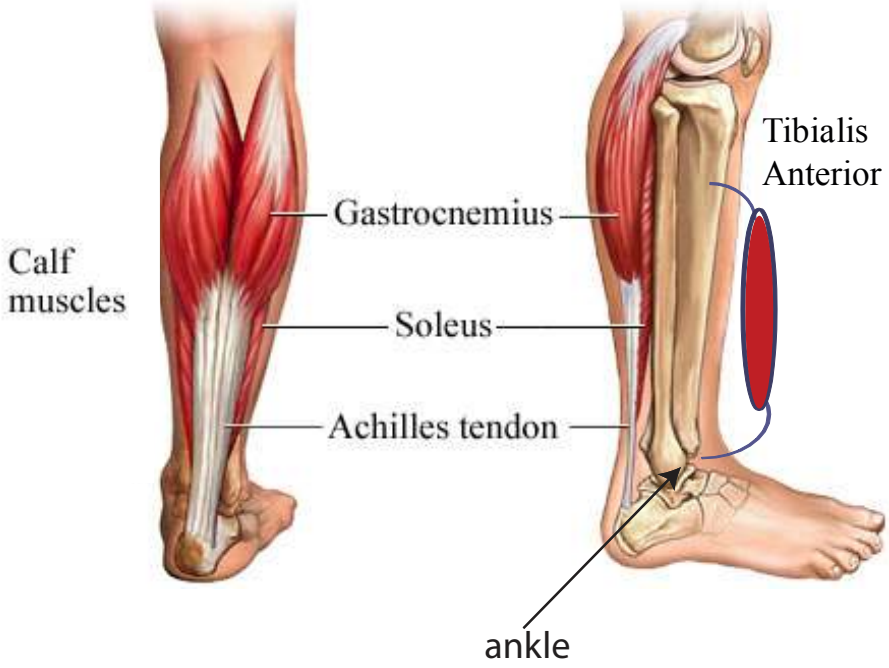

Figure 2-2: Muscles and Tendons of the Ankle-Foot Complex

The Triceps Surae comprises the two heads of the two major masses of muscle in the posterior part of the lower leg. The two muscles are Soleus and Gastrocnemius, with the latter having two heads (medial and lateral). These muscles insert into the bone of the heel of the foot (Calcaneus). Commonly they are referred to as the calf muscles. The Tibialis Anterior muscle is located in the anterior part of the lower leg. Finally, there is the Achilles tendon (ACHI) - known to be the largest and strongest tendon in the body. This mass of tendinous structures connects the Calcaneus with both the Triceps Surae muscles.

All the muscle-tendon units are unidirectional actuators, and can cause two kinds of motion at the ankle joint: plantar flexion and dorsiflexion. Plantar flexion is a motion of the foot rotating the forefoot away from the shin. Plantar flexor refers to a muscle that causes plantar flexion. Dorsiflexion is the reverse of plantar flexion; and rotates the forefoot upwards towards the front of the shin. Dorsiflexor refers to a muscle that causes dorsiflexion.

Of the major muscle-tendon units outlined above, the Soleus (SOL) and Gastrocnemius (GAS) are the major plantar flexors, and the Tibialis Anterior (TA) the major dorsiflexor. There are smaller plantarflexors[1] and dorsiflexors[2], that are not

[1]Flexor Longus muscles, Posterior Tibialis, the Peroneus Longus and Brevis muscles
[2]Extensor Hallicus Lingus and Extensor Digitorum Longus

considered individually in this thesis. Their effect is lumped into the effects of the bigger muscles in their categories.

2.3 Muscle Physiology

This section (a) describes the process of actuation of skeletal muscle and (b) introduces qualitative and quantitative aspects of features affecting muscle dynamics.

2.3.1 Structure

Skeletal muscles are highly structured. Structural units in order of increasing granularity are muscles, fascicles, fiber bundles, muscle fibers (cells), myofibrils, myosin and actin filaments. Muscles contain fascicles, and fascicles contain fiber bundles and so on. The myosin (thick filaments) and actin (thin filaments) are hexagonally arranged.

2.3.2 Force Generation

Muscle is a tension actuator controlled by nervous system signals. Nervous impulses are conveyed to muscles at the neuromuscular junction via firing of efferent motor neuron action potential trains (a series of all or none pulse-events). These action potentials set off a depolarization wave that invades muscle cells via transverse tubules. This invasion depolarizes the membranes of the muscle's calcium stores - sarcoplasmic reticula (SR) - causing the release of calcium ions from the SR into the cell interior. The calcium ions then bind to a protein (troponin in the troponin-tropomyosin complex) that sterically blocks myosin binding sites on the actin filament in resting muscle. The calcium binding with this complex causes a conformational change, exposing the myosin binding sites on the actin filament. This allows myosin heads to bind with actin, and causes the formation of 'cross-bridges'.

The cross-bridge formation releases energy stored by myosin. This causes the myosin molecule to relax by rotating its globular head, which in turn induces the filaments to slide past each other longitudinally. The formation of cross-bridge bonds stiffens the muscle, helping it generate force by a mechanism similar to that involved in connecting many stretched springs. The sliding of filaments during force generation imposes a length-dependence on this stiffness. Further, since it takes a finite amount of time to attach, if filaments are sliding past each other at high velocity, lesser cross-bridges will be formed and less force will be generated. This can be interpreted naively as a variable 'viscosity' feature of the muscle dynamics, and was explained by A.V. Hill through difficult and famous thermodynamic experiments relating speed of shortening, rate of energy release, and muscle force [12]. A key feature of the force-velocity relation is that the slope during slow lengthening is around six times greater than that during slow shortening.

After the action potentials cease to fire, the calcium ions get taken back into SR stores. The decrease in free calcium ions reverses the protein complex changes,

causes breakage of cross-bridges between actin and myosin filaments and causes force to cease.

2.3.3 States and Dynamics

The force generation described above is often described as contraction dynamics of the muscle. For a systems description of these dynamics, it is important to identify and define the three states of muscle influencing contraction: activation, length and contractile velocity.

Activation: The muscle active state or 'muscle activation' is defined in the literature as the relative amount of calcium bound to troponin [13, 14]. The significance of this binding to force generation is apparent from its role in cross-bridge formation as outlined above. For a systems level description, the active state is an 'average' property of a set of fibers that are excited asynchronously by neural pulse-trains [15]. Therefore, it is an indicator of the relative number of exposed myosin binding sites on the actin filaments, or in other words the relative [3] number of cross-bridges that can be formed at a specific time-point. A muscle's active state describes the (relative) level of its force-generation capability commanded by the nervous system.

Length: This is the length of the muscle fascicles. The dependence of muscle dynamics on length is a bell-shaped tension-strain curve that comes about from the sliding filament theory discussed above.

Contractile Velocity: This is the rate of change of fascicle length during contraction. The dependence of muscle dynamics on velocity comes from the 'viscous' effects discussed above. Based on muscle velocity, force generation of muscle is divided into three modes: (a)isometric mode referring to zero-velocity, constant length force generation, (b)concentric mode referring to negative velocity or shortening contraction, (c)eccentric mode referring to positive velocity or force generation in which fascicles lengthen.

All three muscle states affect muscle impedance (effort to flow relation) -as the dynamics (relating motion to force) depends on each of the three states. Muscle models formalize the state-dynamics dependencies.

2.3.4 The Hill-type Muscle Model

One of the most widely accepted models of muscle dynamics is the Hill model. This model is based on several empirical studies, and models muscle contractile force F_{CE} as a multiplicative effect of functions of each of the three states.

$$F_{\mathrm{CE}}(t) \propto \alpha(t) \cdot f_l(l_{\mathrm{CE}}(t)) \cdot f_v(\dot{l_{\mathrm{CE}}}(t)) \tag{2.1}$$

α is activation and l_{CE} is muscle (contractile element) length. f_l and f_v denote the length and contractile velocity dependencies of contractile force respectively. Hill models also include a non-linear parallel elastic term representing the elastic struc-

[3] relative to maximum number of cross-bridges that can be formed in the muscle at any time

tures (collagenous fibers) encompassing the muscle. The total force generated by the muscle is $F_{\mathrm{m}} = F_{\mathrm{CE}} + F_{\mathrm{PE}}$.

The Hill model assumes the active state to be independent of the fascicle length and velocity. There are other models like the Distribution Moment model [14, 16] which detail complex interactions between the activation and length/velocity states as well. For our purposes, the Hill model was chosen for its elegance and simplicity. With a small number of parameters defining the dynamics, this model captures impedance and operation regimes pertaining to most functions of skeletal muscle - ranging from actuator, clutch, strut to brake.

2.4 Tendon Physiology

This section describes qualitative and quantitative aspects of tendon structure, dynamics and function.

Tendons are masses of passive, connective tissue connecting muscle to bone. They attach to muscles in oblique series arrangements (at angles termed pennation angles[4]), to exert pulling forces when the connecting muscle(s) are active. They are composed of parallel arrays of collagen fibers packaged together. As such, tendon structure mimics the parallel elasticity described above.

The tendon elasticity is non-linear, with a length-tension curve that is an offset exponential [17, 18, 14].The tangent modulus of elasticity increases with strain at low strain and stays approximately constant with strain at higher strains. Tendon action is governed by parameters related to its structure or morphology such as slack length, cross-sectional area and reference strain. The reference strain depends on the ratio of muscle to tendon cross-sectional areas. While most models of tendon are lossless, animal tendon has been shown to lose upto 6-11% of its stored energy due to viscosity during shortening at physiological rates [17, 14].

The main function of tendon is to transmit force between muscle and load, like gears in a bicycle. Tendons also mediate the transfer of information about mechanical effects at the load to the nervous system. Abstractly, tendons link the load and the actuator, and affect the impedance seen by the actuators. As such they can modulate the effect of muscle actuation.

2.5 Neural-Structural Interactions

It is apparent from Figure 2-3 that tendon morphology and neural commands both affect muscle dynamics and muscle state.

- Tendon morphology represents the passive, structural effects on muscle state. Tendon structure affects tendon dynamics, and in turn the muscle dynamics by affecting muscle length and velocity.

[4]Greater pennation angles mean better transmission of muscle force, and less muscle force needed for a given movement

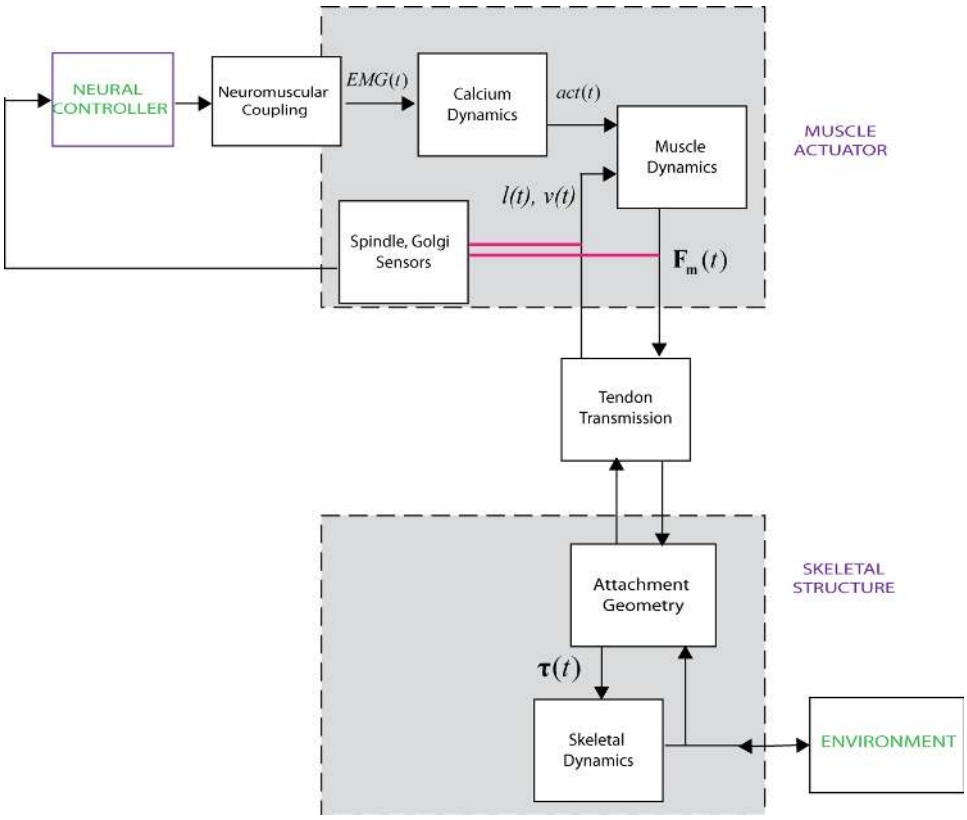

Figure 2-3: Placing neural control, muscle actuation, tendon transmission and environmental perception in the hierarchical context. Artwork courtesy Cajigas 2009.

- Neural commands represent the active effects on muscle state. They affect contraction dynamics, and in turn the muscle dynamics by affecting muscle active state.

Therefore, interactions between neural control and features of leg structure are manifested in the muscle state evolution.

Implicitly, this means that the interplay we seek to understand is manifest in muscle impedance modulation. Since neural commands sometimes convey 'intent' to the limb and tendinous structures sometimes transmit environmental effects to the nervous system, muscle impedance changes result from and mediate both 'intent' and 'feel'. Thus, to understand the interactions between the two aspects, we must first understand muscle impedance modulation. Equivalently, we must estimate the common denominator affected by both neural and structural aspects - the muscle state evolution.

2.6 Problem Statement

This is a good place to add some depth and perspective to the thesis problem introduced in Chapter 1, in light of the background described here. The arguments presented above suggest reframing the inverse problem to capture neural-structural

interactions from gait data, into the inverse problem of estimating muscle state from gait data. Now we can pose the mathematics of this latter problem for ankle joint motion.

$$\begin{aligned}
\tau(t) &= \sum_i (F_i(t) r_i(t)) && (2.2)\\
F_i(t) &= F_{\mathrm{m},i}(t) = F_{\mathrm{t},i}(t) && (2.3)\\
F_{\mathrm{m},i}(t) &\propto \alpha_i(t) \cdot f_l(l_{\mathrm{CE},i})(t) \cdot f_v(\dot{l_{\mathrm{CE},i}})(t) + F_{\mathrm{PE}}(l_{\mathrm{CE},i}) && (2.4)\\
F_{\mathrm{t},i}(t) &= f_{\mathrm{t}}(\lambda_i(t), \vec{m}_i) && (2.5)
\end{aligned}$$

The first equation expresses net ankle torque as the sum of individual muscle-tendon unit torques. $F_i(t)$ is the muscle-tendon force, which is equal to both the muscle force $F_{\mathrm{m},i}$, and tendon force $F_{\mathrm{t},i}$. $r_i(t)$ is the time varying moment arm of muscle tendon unit i. The second equation describes the kinetics of the non-linear system formed by each individual muscle-tendon unit. The third and fourth equations are for the non-linear functional forms of muscle and tendon. $\lambda_i(t)$ refers to tendon strain, which is related to $l_{\mathrm{CE},i}(t)$ by the structural features and geometry of the muscle-tendon attachments for unit i. Therefore, λ_i is implicitly known if $l_{\mathrm{CE},i}$ is known. $\vec{m}_i$ refers to the morphological parameters governing the tendon force-length relation f_{t}.

All in all, there are three independent unknowns $(\alpha_i, l_{\mathrm{CE},i}, \vec{m}_i)$ for each muscle-tendon unit i. The first two are hidden state time series variables, and the last unknown $\vec{m}_i$ represents time invariant structural features governing f_{t}.

The system has many degrees of freedom within each muscle tendon unit. The summation imposes yet another redundancy on the inverse problem of inferring individual muscle-tendon effects from overall joint torques. The inverse problem of constraining these degrees of freedom to obtain muscle state from data reduces to (a) estimation of hidden states α_i and $l_{\mathrm{CE},i}$ and (b) system identification of $\vec{m}_i$ for each muscle-tendon unit i spanning the ankle. The next chapter details the methods we used to solve this inverse problem.

Chapter 3

Methods

Several empirical and mathematical techniques were employed to obtain data-driven ankle muscle state estimates, while capturing key aspects of both neural control and leg structure in walking. Standard empirical techniques were used to collect heterogeneous motion datasets on healthy adults. The kinematic and kinetic data were processed to obtain gross information (angles and torques) about joint motion. Standard gait analysis methods were then employed on the joint angles to estimate muscle-tendon unit state. Using this information and the electro-myographic data, underlying muscle states were estimated in a two-step fashion. First, a Bayesian inference algorithm was used to obtain individual muscle activation estimates from the EMG data. Second, key morphological parameters influencing muscle function and energetics were identified with an optimization scheme. This chapter provides a detailed description of each of these steps: (a) data collection, (b) data processing for ankle joint and muscle-tendon state, (c) estimation of ankle muscle state using EMG data and a musculoskeletal model-based system ID procedure.

3.1 Data Collection Procedures

Kinetic, kinematic and electro-myographic data were collected at the instrumented Motion Analysis Laboratory (Holodeck) in the Computer Science and Artificial Intelligence Lab (CSAIL) at MIT, in a study approved by the MIT Committee on the Use of Humans as Experimental Subjects. Five healthy adult males participated in the study. Care was taken to ensure that the subjects did not suffer from known gait pathologies, injuries and leg length asymmetries. The range of anatomical dimensions, ethnicities and athletic abilities represented in the study are detailed in Table 3.1.

After obtaining informed consent, the participants were asked to walk barefoot at a self-selected speed (typically around $1.25 - 1.35\,\mathrm{m/s}$) across a $6\,\mathrm{m}$ walkway in the Holodeck. Walking speeds within 5% of self-selected speed were accepted. For each study participant, a total of 25-30 trials were collected.

Table 3.1: Subjects for Motion Capture Data Collection

Subject Initials	Age [yrs]	Weight [kg]	Height [in]	Leg Length [in]	Gender	Ethnicity	Athletic Ability
JS	21	81.8	75.5	40.6	Male	White	Moderate
KE	31	77.8	72.0	36.6	Male	Japanese	Moderate
RS	26	72.7	73.0	40.9	Male	South Asian	Basic
EJ	21	72.0	67.0	34.2	Male	Korean	Professional
AS	24	86.4	71.0	38.4	Male	East Indian	Basic

The data collection procedures were based on standard techniques. Three kinds of data were collected synchronously:

Kinematic Data: An infrared camera system (16 cameras, VICON motion analysis system, Oxford Metrics, Oxford, UK) was used to measure three-dimensional locations (with precision of about 1 mm) of reflective markers at 120 Hz. The markers, 13 mm in diameter, were placed at 46 (bilateral) locations on the participant's body (as per the prescription of the Helen Hayes marker model) to track the subject's motion during the trials.

Kinetic Data: Two back to back platforms (Advanced Mechanical Technology, Inc., Watertown, MA) embedded in the walkway were used to measure ground reaction forces synchronously with the kinematic data at a sampling rate of 1080 Hz. To ensure natural gait, subjects were kept blind to the force-plate locations. The platforms measured ground reaction force and center of pressure locations to precisions of about 0.1 N and 2 mm respectively.

Electro-myographic Data: Surface EMG from the Soleus, Medial Gastrocnemius, Lateral Gastrocnemius and Tibialis Anterior muscles from one randomly chosen leg was also recorded synchronously at sampling rate of 1080 Hz. A 16 channel EMG system and MA-411 preamplifiers (20X gain) from Motion Lab Systems were used for surface EMG measurements. The EMG data collection was done in the presence of a physician, using disposable, pre-gelled surface bipolar electrodes with 20 mm center-to-center spacing (Electrode Store Model BS-24SAF, part # DDN-20).

To test robustness of modeling and estimation procedures, data was collected on two days for two of the five subjects. Consistency of the procedures and calibrations performed on separate days was ensured.

3.2 Data Processing

3.2.1 Joint State

Information at the joint level is, physiologically, the coarsest description of limb movement possible. Therefore, analysis of joint state serves as a good starting point for an inverse problem. This section summarizes the steps taken to obtain joint mechanical state (angle and torque) from raw marker and force plate data.

Raw marker data was labeled and gaps in marker locations were filled using the interpolation algorithm in the VICON motion capture software. The VICON motion capture data was then exported into SIMM (Software for Interactive Musculoskeletal Modeling, MusculoGraphics Inc., Evanston, IL) using the SIMM C3D Module. SIMM was chosen for analysis of joint state because of (a) the anatomical accuracy in representing complicated joints and skeletal structures and (b) the ability to access subject-specific parameters used in the calculation during modeling for consistency.

Inverse kinematics and inverse dynamics analyses on the data were performed in SIMM to obtain joint angle and torque time series. The SIMM Full Body Dynamic Model was used as the template for inertial, geometric and mechanical properties. This template model was scaled to subject dimensions using algorithms within SIMM. The marker data were digitally filtered using fourth-order zero-lag Butterworth filters. The cut-off frequency was 10 Hz. Forces were not smoothed as the sampling rate was high. Inverse kinematics was performed in SIMM to find joint angles. The algorithm uses marker trajectories and internally pre-defined anatomical landmarks to find instantaneous joint centers, and then calculates joint angles from these center points. Equipped with the joint angles and the measured ground reaction forces, it is possible to perform inverse dynamics and find the joint torques generated by the subject during the trial. The inverse dynamics analysis was performed using the SIMM Dynamics Pipeline to obtain joint torques, segment and full body center of mass positions as a function of time.

Since each trial normally comprised multiple gait cycles, data for individual gait cycles was extracted by identifying gait cycle start and end points. These points were estimated using sudden changes in ground reaction force and repeating patterns in heel marker position. To prevent errors in gait cycle start and end point definition from propagating into the estimation and model identification steps, systematic errors were corrected as follows. All processed data was circularly shifted to optimize the simultaneous periodicity of the ankle, knee, hip joint angle and torque gait cycles. Typically, this meant a circular shifting of 2-5 points out of 100. The data was then time-normalized to percent gait cycle co-ordinates. Figure 3-1 shows the sagittal plane ankle angle and ankle moment averaged across all trials for each subject.

Only one degree of freedom ankle motion and dynamics were considered for our analysis, since most of level ground walking is known to occur in the sagittal plane. Forward progression speed in the sagittal plane and stride length were calculated using the full body center of mass position trajectory obtained from the inverse dynamics. Timing of significant gait events such as toe-off (stance-end) and contra-lateral heel strike were calculated from patterns in changes of force measurements and heel/toe

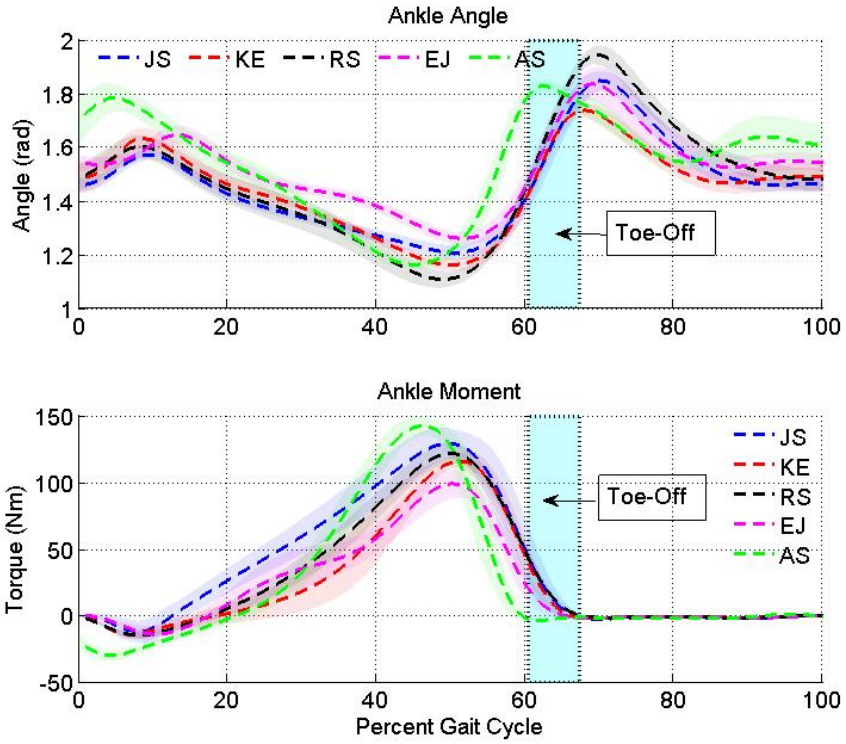

Figure 3-1: Ankle angle and moment for 5 subjects. Averages are from steady state gait cycles. Standard deviation indicated is across multiple walking trials for a given subject. Average steady state speed across subjects was 1.25 m/s.

marker positions. Typically toe-off occurs around 50-80% of gait cycle - when the ankle moment transitions from positive to negative (plantar flexion to dorsiflexion).

3.2.2 Muscle-Tendon State

To transition from joint state to individual muscle state, it is necessary to first obtain the muscle-tendon unit state. Joint angle trajectories are related to the muscle-tendon unit lengths via the geometry of the musculoskeletal system. This section outlines the procedures followed to obtain muscle-tendon state from joint state.

The literature is rife with several geometrical models that have been used to estimate muscle-tendon lengths from joint angles. For our estimation, we chose the SIMM Full Body Dynamical Model introduced in Section 3.2.1, as it is widely accepted as a professional standard in the field. This model is unique in its level of anatomical detail and accuracy. In particular, it integrates digitized bone surface data with cadaver data to define points where muscle wraps over bone. This enables the model to capture variations in muscle paths and lines of muscle-tendon action arising from the complex musculo-skeletal geometry [19].

For the actual calculation of muscle-tendon length from joint angle, we followed SIMM's method as it is well suited to the geometrical model. Briefly, the inputs

to the estimation algorithm are the joint angles obtained from inverse kinematics and the musculoskeletal parameters scaled to the subject dimensions. The software performs a co co-ordinate transformation to the individual muscle frame defining muscle path, to compute muscle-tendon length. The algorithm is detailed in [19]. We also obtained estimates of the moment arms ($r(t)$ in Equation 2.2 from the same model for consistency, for use in the system ID step to be described in Section 3.5.

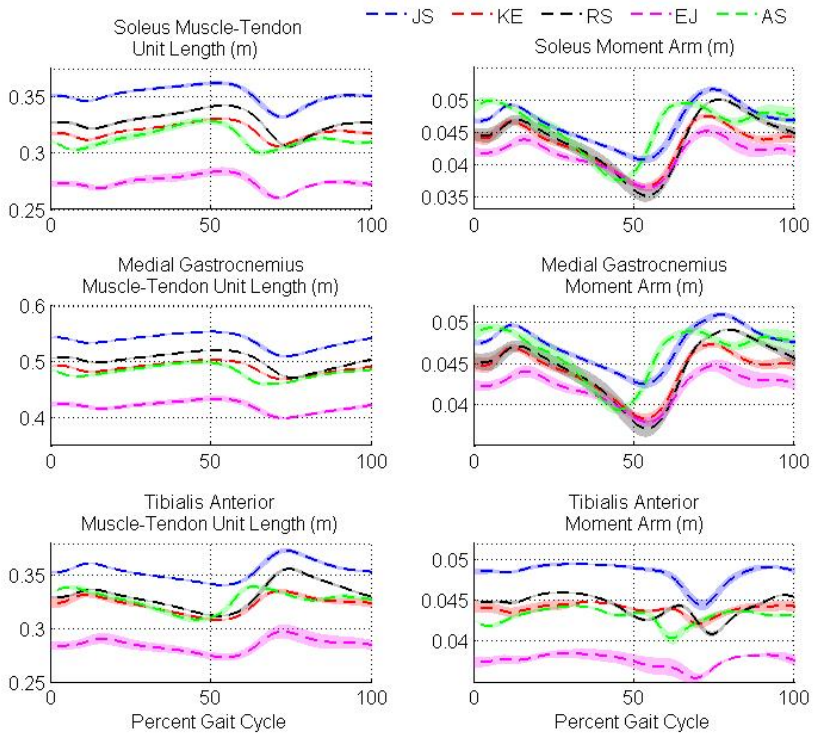

Figure 3-2: Muscle-tendon unit length and moment arms for 5 subjects. Same time normalization and averaging as for joint state.

The plots in Figure 3-2 show averages of right and left estimates obtained using SIMM for all trials on each subject. The averaging accounts for disparities in left and right muscle parameters that may have arisen during scaling of the template model.

Summarizing briefly, we have detailed in the previous two sections the many standard gait analysis procedures employed to (a) collect in vivo motion data and (b) to use the data for calculation of joint state and muscle-tendon length profiles. We now have some base information to build the estimator of muscle state referred to in Section 2.6.

3.3 Estimation of Muscle State

While joint angles can help estimate the geometry of the muscle-tendon unit as a whole, joint and muscle-tendon mechanical state by themselves do not uniquely specify the state of individual muscles and tendons. This is because of two reasons:

1. Most joints (including the ankle joint discussed here) are over-actuated with many muscle actuators spanning them and multiple muscles can be simultaneously activated.

2. Further muscle-tendon unit state cannot be directly related to muscle state without knowledge of the morphology governing tendon action.

To address these respective redundancies, we need phase and amplitude information about neural control at the individual muscle level as well as the tendon morphology governing muscle action within the muscle-tendon unit. We evolved a two-step framework to address these aspects by:

1. Analyzing EMG data for neural control at the individual muscle level via a hidden state estimation

2. Obtaining key morphological parameters affecting muscle state within the muscle-tendon unit via a system identification procedure

The next two sections detail our two-step method for estimating individual muscle state from the EMG data and the joint/muscle-tendon unit states.

3.4 Neural Control to Individual Muscles

Among all the information recorded during the human trials, the EMG data is the only piece that directly relates to neural control commanding individual muscle activity. Therefore it is valuable in addressing the redundancy challenge arising from co-activation of multiple muscles. The next few subsections describe (a) the biophysics of the coupling between neural commands, muscle activation and EMG data, (b) the method we evolved from those in the literature to estimate muscle activation from EMG data, (c) our implementation algorithm and (d) the results of our estimation.

3.4.1 Biophysics of Muscle Activation

Before using the information in the EMG data to infer neural control commanding muscle activity, it is important to understand the biophysics associated with muscle activity and the nature of the information contained in the EMG signal. Figure 3-3 provides a systems view of the important information about muscle activation biophysics from Chapter 2.

The neural action potential train is a spike-like process that commands the muscle active state via excitation, activation and deactivation dynamics.

Neural excitation can be viewed as a jump process causing release of calcium ions from the sarcoplasmic reticulum (SR). The jumps can be physically related to sourcing of calcium ions. Implicit to this jump process are all the non-linear dynamics governing motor unit recruitment and firing patterns - which are blanketed into neural excitation jump process in this thesis. It is known that the relative increase in calcium

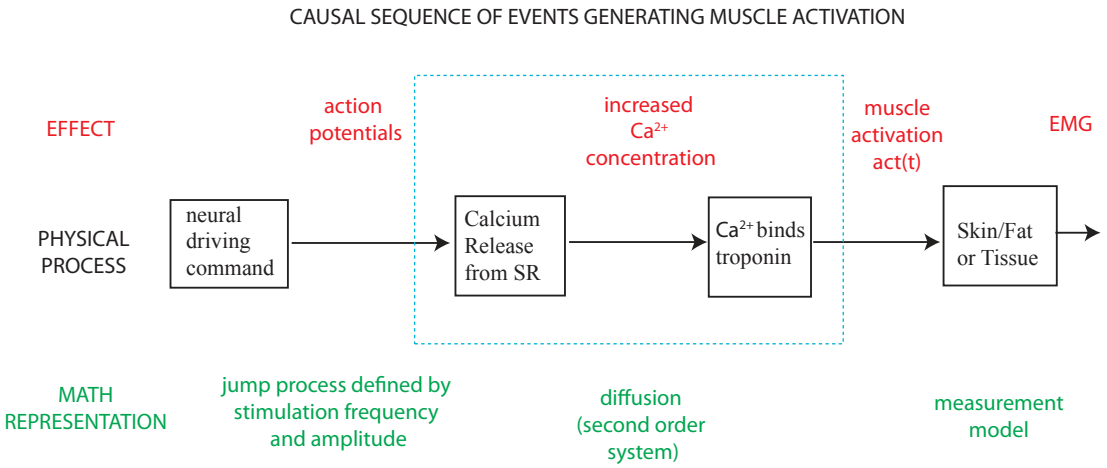

Figure 3-3: Biophysics of muscle activation.

ions in response to a stimulus depends on the history - i.e. the pre-stimulus free calcium concentration [15].

Activation dynamics refers to the link between the neural excitation process and the active state. It comprises the calcium-troponin binding dynamics dictating cross-bridge formation, and involves a series of slow, 2nd order events, rate-limited by biochemical reaction rates (especially the calcium-troponin binding kinetics), ion diffusion rates and field-induced (drift-like) ion currents. Activation can be viewed as a slow-diffusion like process driven by the jump process sourcing calcium. The activation reaches its peak $10 - 12\,\text{ms}$ after stimulation frequency increases from basal levels [15].

Finally, the deactivation dynamics refers to the process by which calcium ions get taken back into the sarcoplasmic reticulum when action potentials cease to fire. Thus fall in excitation is like a sink of calcium ions. The decrease in free calcium ions causes unbinding of calcium-troponin, a fall in the active state, and reestablishes inhibition of cross-bridge formation by the troponin- tropomyosin complex. Typically deactivation time constants are slower than activation time constants. The rate limiting factor in deactivation may be the uptake of calcium into the sarcoplasmic reticulum [20].

The EMG recording is an electric potential measurement. Therefore electromyography senses, through the filter of skin and fat tissues, the net effect of the various pulse-like signals, depolarizations and calcium currents occurring as a result of the neural commands causing muscle activation. Thus EMG data contains phase and amplitude information pertaining to the net active state of the muscle - which is an indicator of the effective neural command at the individual muscle level. This is well acknowledged in the literature with many reported attempts to infer muscle activation from EMG data. The upcoming section reviews some of these attempts, and motivates our approach to this estimation problem.

3.4.2 Estimation of Muscle Activation

Many mathematical approaches have been proposed in the literature for using EMG data to estimate muscle activation. While the fancier techniques attempted range from statistical factor-graph models and autoregressive filters to black box approaches such as pattern recognition and neural networks, the simpler techniques are most widely used.

The most common approach is based on the notion that the amplitude envelope of the demodulated EMG signal is a measure of muscle activity, as the latter is a slow process compared to the spiky neural excitation events captured in the EMG. The amplitude envelope is often extracted by applying a low-pass filter on the full wave-rectified EMG signal. This technique is founded in studies that showed the maximum likelihood estimate of the amplitude envelope could be obtained by low-pass filtering the power in the EMG signal [21, 22].

While the low-pass filter technique is simple and elegant, it cannot resolve sudden jumps in activity or the spike-like nature of the events causing muscle activation. Sanger 2007 [23] introduced an innovative Bayesian estimation algorithm that attempted to sharpen time-resolution. Sanger models the excitation process as a diffusion process driven by a jump process.

$$dx = \epsilon(dW) + (U - x)dN_\beta \quad x \text{ uniform when jump} \tag{3.1}$$

Even though Sanger makes no claims to the physical relevance of his technique, his model reflects the basic excitation biophysics outlined in Section 3.4.1. An easy way to see this relevance is to initialize $x(0)$ as N units. These N units of $x(t)$ will diffuse around till an excitation (frequency β) has a source or sink influence on $x(t)$. Then the new $x(t)$ will diffuse around and so on. The diffusion process comes in between jumps, and therefore is driven by the jumps.

The stochastic model of the underlying process and the Bayesian technique means the approach can capture statistically important features of both the underlying process, and the randomness inherent in the EMG measurement itself. For this latter part, Sanger models the skin/fat tissue filter between actual electrical events in the muscle and the EMG recording through a probabilistic measurement model.

$$P(\text{emg}|x) = \frac{\exp(-\text{emg}|x)}{x} \tag{3.2}$$

The key feature of the measurement model is the Supra-Gaussian nature of the conditional probability density function coming about from the x in the denominator. This feature comes about due to a Laplacian model of the conditional of EMG signal given x, and the rectification of EMG. The Sanger approach propagates the above models of excitation and observation using an approximate solution to the Fokker-Planck equation and Bayes law, to obtain a recursive estimator of x.

A key limitation of using the Sanger model of the underlying process for estimating muscle activity is that it [1] does not capture two important biophysical features

[1] like the linear low pass filter model

outlined above. While Sanger's article did not claim biophysical interpretations, we draw these inferences because they are important for our purpose of muscle state estimation.

1. Firstly, the Sanger model has constant jump frequency and uniformly distributed jump amplitude. Therefore, it does not model the history dependence in the rise and fall of active state. The lack of history effects causes the algorithm to find a sudden jump in the estimated activation when the EMG signal bursts into high amplitude firing, and then mainly diffusion when the EMG signal remains high, and a sudden downward jump when the EMG stops firing. Thus Sanger appears to be estimating the release/flow of calcium in the muscle, and not the active state of the muscle because there are no explicit activation dynamics in his model.
2. Secondly, the Sanger model has the same jump rate for source and sink or for activation and deactivation. This is not consistent with the kinetic differences between the two processes (Section 3.4.1). It is especially important that the deactivation rate is much longer than the activation rate because it means the muscle is generating force for a significant period of time even after the EMG signal dies down. Thus this drawback can cause the estimation of muscle length, velocity and force in our inverse problem to go astray.

The ideal scenario would be to incorporate time varying activation and deactivation rates into Sanger's jump-diffusion process and re-derive his algorithm. However, there is no appropriate analytical solution for the Fokker-Planck equation in the time varying rate case, and it would be necessary to use Monte Carlo simulation techniques for a solution.

A simpler alternative is to assume that Sanger's x corresponds to calcium levels or neural excitation, and then find the active state α by applying calcium-activation dynamics on the x from Sanger's method. A mechanistic model of the calcium-activation dynamics is given in [17], and has the following deterministic bilinear form:

$$\frac{d\alpha(t)}{dt} + \left[\underbrace{\frac{1}{\tau_{\text{act}}}(\gamma + (1-\gamma)x(t))}_{\text{rate constant}}\right]\alpha(t) = \frac{1}{\tau_{\text{act}}}x(t) \qquad 0 < \gamma = \frac{\tau_{\text{act}}}{\tau_{\text{deact}}} < 1 \tag{3.3}$$

This model accounts for the two effects missing from the Sanger specification. The history dependence is modeled by the dependence of rate on $x(t)$. A higher $x(t)$ would mean that the rise rate of the activation $\alpha(t)$ is higher. Further the different activation and deactivation rates are captured in parameter γ which is defined as the ratio of activation to deactivation time constants. There are instances in the literature where the bilinear model is used by itself, by setting $x(t) = |\text{EMG}|$. We chose a hybrid of the Sanger-bilinear model because the bilinear model by itself does not capture statistical features in the data, and ignores the information contained in the randomness of the signal. Our implementation of this hybrid approach is outlined below.

3.4.3 Implementation Algorithm

The algorithm has 4 main parts: (a) pre-processing, (b) statistical technique, (c) artifact removal and (d) activation dynamics. All of the steps were followed for each individual muscle, unless indicated otherwise.

Preprocess: First, we performed 4 standard pre-processing operations [24]. We removed the DC offset (mean) from the raw EMG data, and calculated the standard deviation (d) in signal. Then we clipped the signal at times when it is greater than $5d$ to remove outliers that may have arisen from artificial effects[2]. We then full-wave rectified to capture 'power'-like features. It is important that rectification comes after the first 2 steps as the rectified signal has a different mean and standard deviation than the raw recording. Finally, we normalized the rectified signal by the peak EMG value during the walking trial.

Statistical Technique: The preprocessed gait EMG data was first analyzed using the Sanger algorithm. The diffusion and jump rates (ϵ and β) were chosen to be similar to the parameters in [23]. It is known that the diffusion of calcium ions should be quite rapid [20, 25]. However, sensitivity to ϵ is low, and it can be varied between $0.001 - 100$ units. It was set to 0.001 units for this study. The jumps take care of what the diffusion cannot and the measurement model helps the estimation a lot. Also, sudden extreme jumps are rare in physical systems, but having a non-zero jump frequency is statistically important. Further, the jump rate sets the time resolution of the model especially during 'turn on' and 'turn off' of the muscle. It was empirically found that β between $10^{-20} - 10^{-30}$ Hz worked well for the gait data, while parameters outside of this range introduced either really jittery estimates or really slow build up of active state. For this study β was set to 10^{-24} Hz as in Sanger's study.

Artifact Removal: Before further analysis, we removed motion artifacts on estimate. This step is intermediate to the statistical and mechanistic steps as applying motion artifact removal on the raw data may cause loss of valuable statistical features. Further, it is easy to discern motion artifacts and their sources, after distilling out the phasic, statistically relevant information from the raw EMG data. It was found (by examining x) that the ankle plantar flexors have motion artifact spikes around the foot-flat period, possibly due to movements of the flabby muscles (and their electrodes). The artifacts should be filtered out to prevent spiking of the estimated activations for these muscles around foot flat to mid-stance. Easy choices for removal are moving average or median filters applied around foot flat (easy to identify using ankle angle patterns). We used a causal moving average with a 100 ms time window. The window was chosen to be just high enough to filter out the artifact without causing loss of information about shape of the activation estimates. The moving average was time varying as it was only turned on between $8 - 30\%$ gait cycle for the Soleus, and $15 - 30\%$ gait cycle for the Gastrocnemius.

[2] $5d$ is 99.999% of the data, if we assume a normal distribution.

Activation Dynamics: With $x(t)$ estimated, we can apply calcium-activation dynamics by solving the equation 3.3 in MATLAB Simulink. The activation and deactivation time constants governing the calcium dynamics were set to average values specified in [14]. The average activation and deactivation time constants for the ankle muscles range between $9-10\,\text{ms}$ and $45-50\,\text{ms}$ respectively[3]. The specific values of the constants do not matter as much as the ratio between the activation and deactivation constants. The time constants were not scaled to be subject-specific, but the muscle-specificity allows the estimation to factor in variations arising from differences in fast-slow fiber compositions of muscles. Since the bilinear equation can amplify the noise floor, we dealt with any noise-floor by setting the minimum value of the activation estimate to 10% of the standard deviation when the muscle is on.

The implementation, like in Sanger's article, was ensured to be causal, recursive and vectorized for efficiency - with a view to real-time applications that will be outlined in Chapter 6. The bilinear differential equation can be implemented using a difference equation in a micro-controller for speed.

3.4.4 Results

Figure 3-4 differentiates the results of the several implementation steps outlined above. The figure shows the effect of the activation dynamics on the Sanger esti-

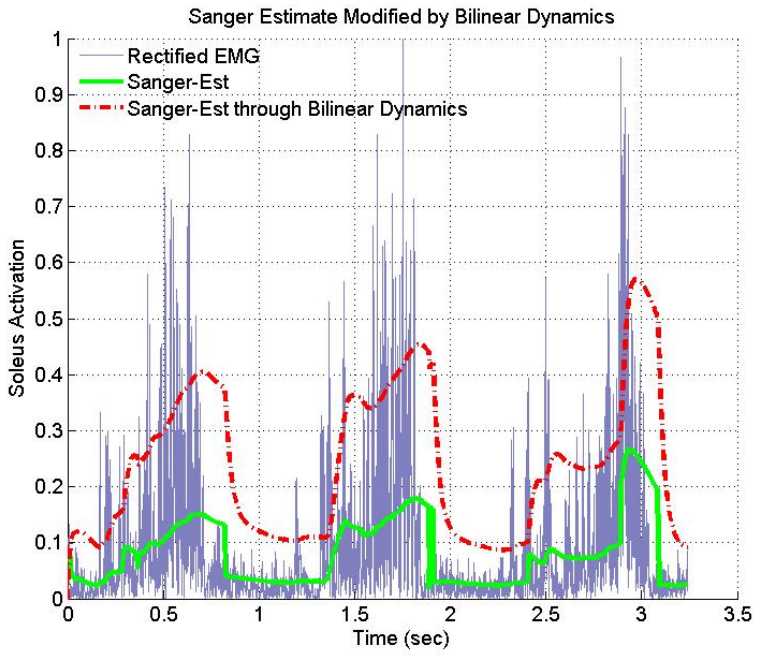

Figure 3-4: Steps between raw EMG data and muscle activation estimate. Gray bursts are preprocessed EMG data, green solid line shows x, and red dashed line indicates α.

mate x (green). The active state α (red) rises much faster than x - highlighting the

[3]Time constants were calculated with reference to firing at the neuro-muscular junction

history dependence of the rise rate. Further the fall in α is slower than the rise showing the difference between activation deactivation rates. The need for the extra rise and the rising time constant offered by the hybrid approach will become clearer in the system ID section (3.5).

The jumps in the jump-diffusion process model help inform the model with both sharp rises in the data as well as firing rate changes (recruitment frequencies). This is a feature that is emergent to trends in the data, that would not arise from simple filters like integrators with fixed or adaptive window sizes.

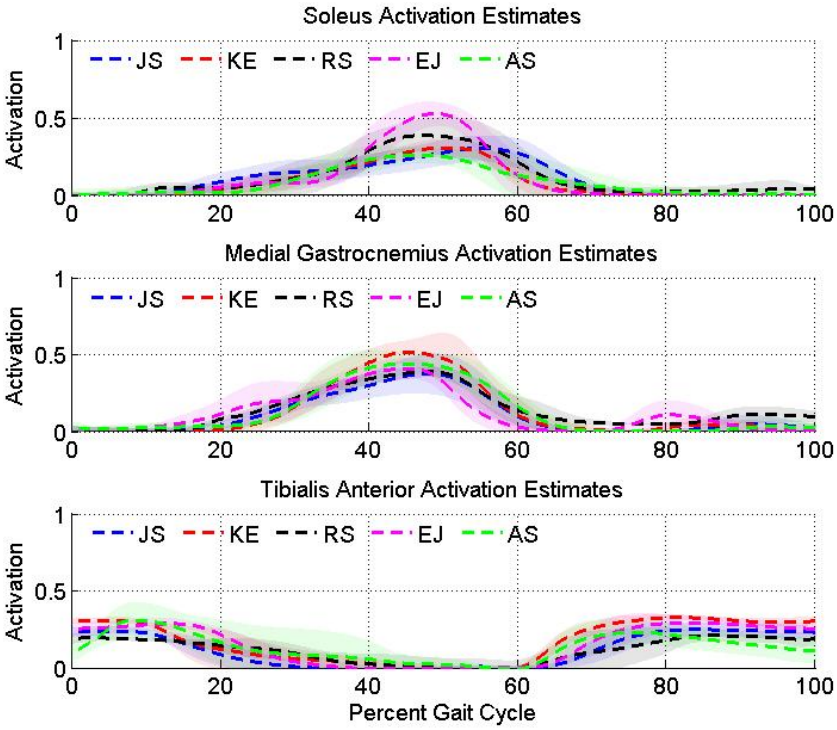

Figure 3-5: Activation estimates for 3 ankle muscles for 5 subjects.

Figure 3-5 shows average estimates (across trials) for each muscle for all 5 subjects. The trial-to-trial variability of phasic trends in the activation estimates is generally low. Variability in amplitude features is low when activation is close to 0, and rises when activation is high. The method appears to capture a repeatable average with as few as 4-5 trials, and even lower in cases of minimal motion artifact.

3.4.5 Active State Estimation Summary

In summary, this section focused on estimating muscle active state from EMG data to overcome the redundancy arising from joint over-actuation and muscle co-activation. We reviewed (mainly three) existing approaches to EMG-muscle activity estimation, and found that current algorithms do not consistently address both biophysical and statistical aspects of the problem. We described the Sanger algorithm ([23]) that

comes close to this consistency, interpreted the biophysical relevance of the approach for our problem, and identified limitations of using the approach as laid out by Sanger. To overcome the limitations, we proposed that the statistical power of the Sanger approach be integrated with mechanistic calcium-activation dynamics for estimation of muscle active state from raw EMG data. Finally we described our implementation of this hybrid approach and the resulting active state estimates.

3.5 Influence of Tendon Morphology on Muscle Action

By obtaining information about the neurally controlled active state of individual muscles, we have addressed the first joint-level redundancy outlined at the start of this chapter. The second muscle-tendon level redundancy needs to be addressed to estimate muscle length/velocity profiles and obtain a complete picture of individual muscle state. For this, we constrained the extra degree of freedom that tendons provide to muscle action within the muscle-tendon complex.

We accomplished this by identifying key tendon morphological parameters through a system ID procedure. The next few subsections describe (a) the system ID problem, (b) the muscle-tendon system models we used, (c) model inputs, (d) the formulation of our approach to the problem, (e) the optimization technique and (f) the results.

3.5.1 System ID Problem

As outlined in Section 2.5, tendon morphology mediates the neural-mechanical link in locomotion. The tendon parameters influencing (a) muscle actuation and (b) communication of perception of load to the nervous system were identified in Section 2.4. Knowledge of these parameters is important to dissecting the length and velocity of the muscle, given the length and velocity muscle-tendon unit (Section 3.2.2).

It is difficult to measure these parameters *in vivo* even though some attempts have been made [26]. As such, cadaver studies are the primary source of information on these parameters. However, the standard deviations on the measurements are rather large, and there is no reliable procedure for subject-specific scaling of any nominal parameters. Therefore, a technique to identify these morphological parameters, in a way that can explain the gait data of a given subject is necessary. To define the problem mathematically, it is important to first describe the system dynamics and available inputs for our system ID problem.

3.5.2 System Model

We defined the system as comprising the major muscle-tendon units contributing to ankle joint rotation in the sagittal plane: the mono-articular Soleus and bi-articular Gastrocnemius [4] plantar flexors, the mono-articular Tibialis Anterior dorsiflexor, and

[4] spanning knee and ankle joints

the Achilles tendon (Figure 3-6).

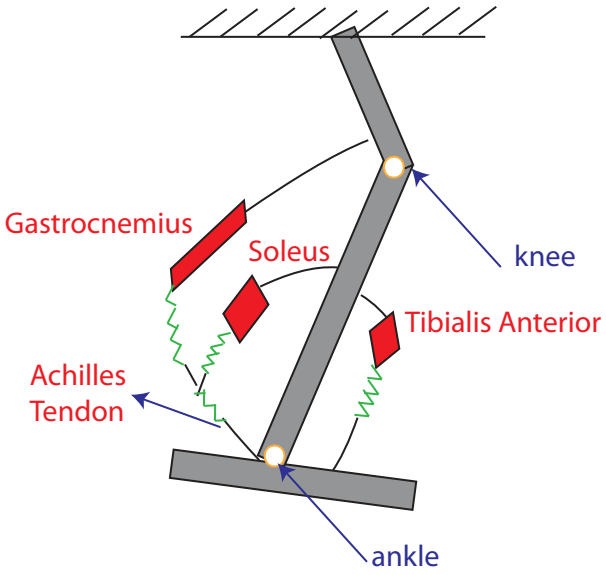

Figure 3-6: Modeled ankle muscle-tendon units. Simplification of Figure 2-2.

Two simplifications of the anatomy drive this system definition:

1. We did not explicitly model the influence of knee muscles and knee joint dynamics on the dynamics of the bi-articular Gastrocnemius muscle. This is reasonable because the problem tackled here is the inverse problem, where the data already represents that coupling and can be used to extract relevant information. Further, the gastrocnemius is known to not transfer much work down from the knee to the ankle [27] and hence its effect at the ankle can be considered in isolation from the knee joint state and musculature.
2. We represented both the medial and lateral heads of the Gastrocnemius muscle as one effective muscle for simplicity, since the two heads act synergistically.

We model the action of the three muscle-tendon units using Hill type muscle dynamics and tendon functional forms from literature as detailed below.

Muscle Dynamics

The concepts governing the Hill type muscle dynamics were reviewed in the Section 2.3. Here we describe our implementation of these dynamics, that is based on that of [9]. The Hill type muscle model contains a contractile element (CE) representing the active muscle fascicle fibers and a parallel elastic component (PE) representing elastic tissue surrounding the contractile fibers.

As in Section 2.3, muscle contractile force is a function of muscle active state α, muscle length l_{CE} and contractile velocity $v_{\text{CE}} = \dot{l}_{\text{CE}}$.

$$F_{\text{CE}}(\alpha, l_{\text{CE}}, v_{\text{CE}}, t) = F_{\max}\alpha(t) f_l(l_{\text{CE}}) f_v(v_{\text{CE}}) \tag{3.4}$$

f_l and f_v are dimensionless relations given below:

$$f_l(l_{\text{CE}}) = \exp\left[c\frac{|l_{\text{CE}} - l_{\text{opt}}|^3}{l_{\text{opt}}w}\right] \tag{3.5}$$

$$f_v(v_{\text{CE}}) = \begin{cases} \dfrac{v_{\max} - v_{\text{CE}}}{v_{\max} + Kv_{\text{CE}}} & v_{\text{CE}} < 0 \\ N + (N-1)\dfrac{v_{\max} + v_{\text{CE}}}{7.56Kv_{\text{CE}} - v_{\max}} & v_{\text{CE}} \geq 0 \end{cases} \tag{3.6}$$

The parallel elasticity introduced in Section 2.6is modeled as a unidirectional nonlinear spring:

$$F_{\text{PE}}(l_{\text{CE}}) = \begin{cases} F_{\max}\left(\dfrac{l_{\text{CE}} - l_{\text{opt}}}{l_{\text{opt}}w}\right)^2 & l_{\text{CE}} > l_{\text{opt}} \\ 0 & \text{otherwise} \end{cases} \tag{3.7}$$

A low limit parallel elasticity (BE) was modeled to handle the unlikely numerical case of the muscle tendon unit becoming slack. This is a numerical tool and not a physical element of the model.

$$F_{\text{BE}}(l_{\text{CE}}) = \begin{cases} F_{\max}\dfrac{2}{w}\left(\dfrac{l_{\text{CE}} - l_{\text{opt}}(1-w)}{l_{\text{opt}}}\right)^2 & l_{\text{CE}} \leq l_{\text{opt}}(1-w) \\ 0 & \text{otherwise} \end{cases} \tag{3.8}$$

The overall force from the muscle is a sum of all these forces:

$$F_m(\alpha, l_{\text{CE}}, \dot{l_{\text{CE}}}, t) = F_{\text{CE}}(\alpha, l_{\text{CE}}, v_{\text{CE}}, t) + F_{\text{PE}}(l_{\text{CE}}, t) - F_{\text{BE}}(l_{\text{CE}}, t) \tag{3.9}$$

Table 3.2: Parameters defining Hill muscle model equations [9]

Parameter	Description	Value
w	width of the bell shaped f-l curve	0.56
c	shape of bell shaped curve near the extremes of the bell	0.05
N	muscle force (in units of $F_{\max}$) at maximum lengthening velocity $v_{\text{CE}} = -v_{\max}$	1.8
K	curvature constant	5

General model parameters defining this implementation are in table 3.2. Muscle specific parameters are as follows:

1. Maximum isometric force $F_{\max}$
2. Optimum fiber length l_{opt} at which muscle provides maximum isometric force

$\alpha \cdot F_{\max}$ for activity level α

3. Maximum contractile velocity of the muscle $v_{\max}$

Tendon Dynamics

As reviewed in Section 2.4, the tendon is a non-linear elastic element in series with the contractile fibers. Of the several approximations to tendon functional form in the literature, we chose the most general one:

$$F_{\text{SE}} = F_{\max} \frac{\exp\left(\frac{K_{\text{sh}}}{\lambda_{\text{ref}}}\lambda\right) - 1}{\exp(K_{\text{sh}}) - 1} \quad \forall \lambda > 0 \qquad \lambda = \frac{l_{\text{SE}} - l_{\text{sl}}}{l_{\text{sl}}} \tag{3.10}$$

F_{SE} is tendon force, l_{SE} is tendon length and λ is tendon strain with respect to slack length l_{sl}. K_{sh} determines the shape of the length-tension curve, and impacts when the tendon force becomes approximately linear in strain. Parameter λ_{ref} is the reference strain at which $F_{\text{SE}} = F_{\max}$.

All parameters defining this tendon model $l_{\text{sl}}, K_{\text{sh}}, \lambda_{\text{ref}}, F_{\max}$ are morphological. l_{sl} and $F_{\max}$ capture the dimensions, cross-sectional areas and space organization in the muscle-tendon unit. λ_{ref} and K_{sh} depend on the material properties and influence tendon stiffness. The upcoming sections detail how these parameters were found.

Muscle-Tendon Unit Dynamics

Since the muscle and tendon are connected in series, at pennation angle θ with each other, the muscle-tendon unit dynamics obey the first-order implicit nonlinear differential equation below:

$$F_{MTC} = F_{SE} = F_m(\alpha, l_{CE}, \dot{l_{CE}}, t)\cos\theta \tag{3.11}$$

$$l_{MTC} = l_{SE} + l_{CE}\cos\theta \tag{3.12}$$

Joint Dynamics

Like in equation 2.2, the overall ankle torque resulting from the three muscle-tendon units in the model is:

$$\tau_{mod}(t) = \sum_i F_{MTC,i}(t) r_i(t) \quad i \text{ refers to muscle index} \tag{3.13}$$

r_i is a time varying moment arm, estimated as described in Section 2.6. Further, the Achilles tendon connecting the Soleus and Gastrocnemius to the heel imposes the following force relation:

$$F_{\text{achi}}(t) = F_{\text{MTC,SOL}}(t) + F_{\text{MTC,GAS}}(t) \quad \forall t \tag{3.14}$$

With the system defined thus, $F_{\text{MTC},i}(t)$ and τ can be calculated if (a) all the parameters are specified, and (b) the $l_{\text{MTC},i}(t), \alpha_i(t), r_i(t$ time series are known. We now

explore system behavior by collating inputs from the literature and our data-driven estimates of joint state, muscle-tendon state and muscle active state.

3.5.3 Inputs to Muscle-Tendon Model

The inputs are of two types: (a) parameters defining the above dynamics models, and (b) estimates of $l_{\mathrm{MTC}}(t)$, $\alpha(t)$, $r(t)$ from the data.

Parameters

First, we input nominal values of all muscle-tendon parameters for an average adult male from literature [19]. The parameters are listed in Table 3.3. The $v_{\max}$ and pennation angles are fixed across all subjects. The l_{opt}, l_{sl} and $F_{\max}$ depend on subject-dimensions, and the nominal values are scaled to subject dimensions. The issue of

Table 3.3: Parameters defining muscle-tendon dynamics [9]

Muscle	$\mathbf{l}_{\mathrm{opt}}$ **[cm]**	$\mathbf{v}_{\max}$ $[\mathbf{l}_{\mathrm{opt}}/\mathbf{s}]$	**pennation [degrees]**	$\mathbf{F}_{\max}$ **[N]**	$\mathbf{l}_{\mathrm{sl}}$ **[cm]**
Soleus	3.0	6	25	4176	26.8
Gastrocnemius	6.4	12	17	$1113 + 488 = 1601$	40.8
Tibialis Anterior	9.8	12	5	603	22.3

scaling muscle parameters to subject dimensions is quite controversial [28]. We chose the scaling algorithm used in SIMM to stay consistent with the algorithms used for inverse dynamics, joint state and muscle-tendon length estimation (as described in Section 3.2.2). This algorithm scales parameter values as follows:

$$\text{subject specific value} = \text{nominal value} \times \frac{\text{nominal muscle tendon length}}{\text{subject specific muscle tendon length}} \tag{3.15}$$

The subject-specific scaled parameters are in table 1. The subject-specific l_{sl} and $F_{\max}$ values are starting points in the identification of the tendon morphological parameters (detailed in upcoming Section 3.5.4).

Since the Gastrocnemius muscle was modeled as an effective representation of the two heads, all parameters were picked for the bigger, more pennate medial head. The only exception was the nominal $F_{\max}$ value - which was set as the sum of medial and lateral head $F_{\max}$'s - to account for the net effect of the two heads.

In addition to the above parameters, the Achilles tendon slack length was also set at 3 cm since literature values for this parameter range from $2-7$ cm. The actual value of this parameter does not influence the muscle dynamics: it is purely a geometric aspect of the model.

Data

Since we desire that morphological parameters identified with our system ID technique be able to explain the gait data of a given subject, it is important to inform the model with the information we gathered from our human studies (Sections 3.1-3.4). As such, we fed in the muscle-tendon length and muscle active state estimated from in vivo data to constrain the $F_{\mathrm{MTC}}(t)$ and the relation between $l_{\mathrm{SE}}(t)$ and $l_{\mathrm{CE}}(t)$.

Since the model is a simplified representation of the *in vivo* mechanics, and the input parameters are set from crudely scaled, average literature values, we thought the model would better cope with average profiles of estimates than with individual trial profiles. Therefore we used the ensemble average profiles of muscle-tendon lengths and muscle activation (Figures 3-3, 3-5) as inputs to the model. Estimates from all steady-state gait cycles in each trial were considered for the averaging to inform the model with lengths and activations best representing a subject's gait.

With these data-based estimates input to the model, there are two independent unknowns in the non-linear muscle-tendon dynamics equations (Section 3.5.2). These are the l_{CE} time series and the time invariant morphological parameters. For a given choice of the morphological parameters, equations 3.11 can be solved numerically[5] to obtain the muscle length, $l_{\mathrm{CE}}(t)$ and muscle velocity, $v_{\mathrm{CE}}(t) = \dot{l}_{\mathrm{CE}}(t)$ that we seek to estimate.

The key question now is how to choose the morphological parameters. As suggested at the start of this section, *in vivo* measurements of these parameters are unavailable and/or unreliable. [29] states that no reliable experimental data exist for tendon slack lengths, and that cross-sectional area measures determining $F_{\max}$ are highly variable. K_{sh} and λ_{ref} for specific tendons are inaccessible and often large ranges are reported from cadaver studies [14]. In the next Section, we introduce an identification scheme for these parameters.

3.5.4 Parameter ID Problem

It is now apparent that the problem of constraining tendon influence on muscle action is mathematically a parameter ID problem. We solve this problem by hypothesizing that neural control and leg morphology have co-evolved to optimize the metabolic economy of level ground self selected speed walking. The optimality of locomotion economy that is the basis of this hypothesis was discussed in Section 2.1.2. With this hypothesis, we can reframe the parameter ID as a data-driven, biologically and physically motivated optimization problem:

$$\vec{m} = \arg\min(\text{net metabolic energy consumed by 3 ankle muscles}) \tag{3.16}$$

$\vec{m}$ is a 14-dimensional vector. Each dimension corresponds to the key tendon morphological features (slack length, reference strain and force, and shape factor) for the three muscle-tendon units, and the Achilles tendon.

[5] We used the MATLAB Simulink implementation in [9] for numerical solutions.

To ensure the morphological parameters can explain the data from human studies, we constrain the parameter ID as follows:

$$|\tau_{\text{mod}}(\vec{m}, t) - \tau_{\text{bio}}(t)| < \tau_{\text{bio,sd}}(t) \quad \forall t \tag{3.17}$$

τ_{bio} is the empirical torque from inverse dynamics on our human subjects. $\tau_{\text{bio,sd}}$ is the standard deviation in τ_{bio}, computed across multiple walking trials for a given subject (Section 3.2.1).

This framing of the parameter ID problem ensures that the tendon morphology captures the following features of the data: (a)dynamic characteristics, (b)neural control, (c) joint and muscle-tendon state and (d) the energetic optimality of self-selected walking. The next couple of sections detail the cost and constraint.

Energetic Cost

There are several approaches in the literature to evaluate metabolic consumption of muscle. Most of them rely on elaborate models of the heats of activation, maintenance, shortening and resting accounting for the many molecular processes involved in muscle force generation [6, 16]. While these models are biophysically quite comprehensive, and can qualitatively match up with empirical data, they have many parameters influencing the cost. Ballpark numbers of many of these parameters exist in the literature, but it is hard to quantify how exactly they vary across muscles and subjects. We chose to avoid the accuracy and sensitivity issues that could arise from a multi-parameter, model-based metabolic cost calculation. Instead, we used an elegant, empirically based cost measure to evaluate metabolic consumption of the muscles in our model.

Empirical studies in isolated muscle have proven that the metabolic consumption of muscle depends primarily on the velocity at which it operates. In fact, it was these empirical studies that defined the Hill type muscle model influencing muscle dynamics[12]. Thus, a cost measure using data from these empirical studies is valuable for our study. Figure 3-7 summarizes empirical relations between muscle metabolic consumption rate and contractile velocity.

The data for shortening came from Hill's original experiments, which have been validated several times and are widely accepted as accurate. The metabolic cost dominates during shortening. For lengthening, we obtained data from biochemical studies of ATP hydrolysis as given in [30]. In general, empirical sources at high lengthening velocities are sparse but the common trends are accepted.

The *in vitro* metabolic power curves in figure 3-7 cannot be integrated as is, to estimate metabolic energy consumed by muscles *in vivo* during natural gait. This is because the data above (and in most empirical plots) is normalized by $F_{\max} \cdot v_{\max}$. This normalization assumes unit activation (or that all cross-bridges are involved in force generation), as most empirical studies are performed *in vitro* under unit activation conditions [16]. *In vivo* operation of muscles during walking, as we know from our estimates in Section 3.4.4, is not at maximal activation. Therefore, to apply the empirical data to gait data analysis, we scaled the metabolic power by activation.

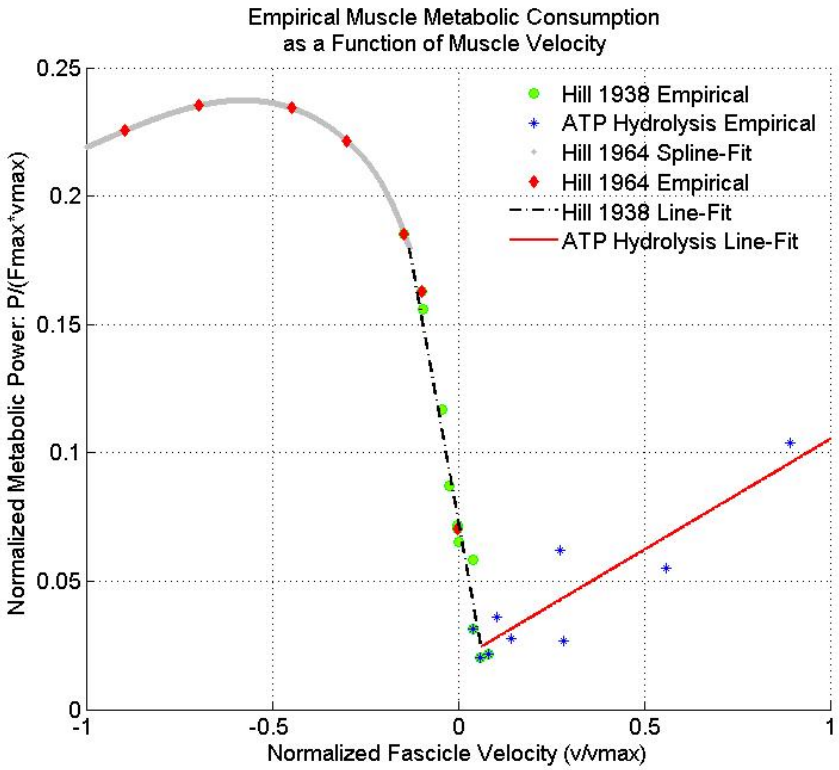

Figure 3-7: Empirically based muscle metabolic power as a function $p(v_{CE})$ of velocity (adapted from [16]).

This is reasonable because the true maximum isometric force of a muscle at any time t is $\alpha(t) \cdot F_{\max}$. When activation is zero, and the muscle is 'off', the metabolic power should be zero (or at basal levels).

Thus, the muscle metabolic cost can be calculated as follows:

$$P(t) = p(v_{\mathrm{CE}}(\vec{m}, t)) \cdot \alpha(t) \cdot F_{\max} \cdot v_{\max} \text{ Metabolic Power} \tag{3.18}$$

$$C(\vec{m}) = \int P(t)\, dt \quad \forall t \text{ such that } \alpha(t) > 0.01 \tag{3.19}$$

Since $v_{\mathrm{CE}}(t)$ is implicitly a function of $\vec{m}$ (due to the muscle-tendon dynamics), C is also a function of $\vec{m}$.

Metabolic power was only accounted for when activation estimates are > 0.01. This was imposed for numerical reasons. When activation is very low, Simulink causes the velocities to spike for a time step or two, after which it rescues itself back to appropriate values. Since the spike in velocity could cause a momentary spike in metabolic power and add artificial cost, we only considered cost when activation built up a little. Further, we found that swing cost is small and rather flat in the parameter space. Therefore, we only calculated C for times t corresponding to the stance phase of the gait cycle.

Constraint and Feasibility

To keep constraint and cost consistent, we implemented the constraint specified in equation 3.17 only over stance phase of the gait cycle. Further, we discounted constraint violations between 0-5% gait cycle as we sometimes found high variability in the estimated inputs during the initial loading phase (probably due to variability in splitting up gait cycles).

The constraint essentially imposes stance phase torque tracking while allowing for the natural variability in the data. Restricting model torque to 1 standard deviation of the empirical torque is like restricting the model-data agreement to $R^2 \geq 0.97$. The feasible region is the set of morphological parameters that can provide human-like torques. We observed that feasibility is mainly a function of phase differences between the peaks of the model input and model torque output.

It may appear striking that the tendon parameters of the biarticular gastrocnemius were constrained only to produce human-like ankle torque, and not to provide human-like knee torque as well. This simplification was motivated by facts indicating that the Gastrocnemius contributes only a small percent of total knee torque[10], as its moment arm at the knee is approximately half the moment arm at the ankle (Figure 3-2). To check, we evaluated feasible sets for the Gastrocnemius tendon parameters satisfying (a) both knee and ankle torque constraints, and (b) only an ankle torque constraint. A comparison found the two sets to be roughly the same, validating our simplification.

There were sometimes cases when the standard deviation in the inverse dynamics torque constraining the model torque output was low but the standard deviations in the muscle-tendon lengths and active state estimates driving the model were higher. A high input variance and a low output variance could make it difficult for the optimizer to chance upon a set of model parameters that are feasible. This was found to be especially true if there was high variability in input phase (e.g. the %GC at which muscle-tendon length started to increase or decrease). The difficulty comes about because our method of feeding in the input estimates from data into the model (Section 3.5.3) did not explicitly account for the variability within the estimates themselves.

To account for variability in input phase, and feed in profiles of the estimates that can best represent the empirical torque output, we performed the following steps:

- We identified points where the standard deviation in input estimate profiles was high.
- Then we evaluated the maximum standard deviation s along the phase axis at these points.

For example, if the average Soleus muscle-tendon length peaked at 54 %GC and if the average $\pm$ 1 standard deviation length peaked at 52 %GC and 60 %GC respectively, we evaluated a maximum phase standard deviation $s = 6$ %GC. Then we iteratively performed circular shifting of the input estimates by 0 to s units to check whether this would help the optimizer find a feasible solution. The circular shifting of input

estimates was applied to all estimates for consistency in designation of start and end of gait cycle.

While this method helped to account for the input phase variability and find feasible regions for all our data, it would be better in a future effort to come up with a better technique to propagate variances within the model.

3.5.5 Implementing Optimization

With cost and constraint defined, we can now describe technical details such as (a) bounds, (b) optimization algorithm, and (c) enforcement of constraint.

Bounds

The choice of bounds was motivated by literature and characteristics of the data. The bounds were made large enough to (a) prevent the optimization from hitting the roof or floor and (b) to ensure feasibility for all subjects. If the range is very large, the optimization will converge very slowly, but that is merely an inconvenience. Some specific considerations that informed the bounds on different parameters are:

- Absolute numerical bounds for the 8 λ_{ref} and K_{sh} parameters are motivated from literature reports [14, 17]. For all the 8 parameters, bounds were set as in Table 3.4 across all subjects.
- Bounds for tendon slack lengths were based on the nominal values listed in Table 3.3. These bounds were derived from the data, so as to prevent muscles from generating force aphysically under slack (i.e. F_{MTC} is never purely from the artificial BE element).
- F_{max} bounds were also based on nominal values listed in Table 3.3. The scaling of the nominal values was set to be large enough to ensure feasibility for all subjects, regardless of height, weight and dimensions.

Table 3.4: Optimization Bounds for Tendon Morphological Parameters

Parameter	Description	Lower Bound	Upper Bound	Model Elements
F_{max} [N]	Muscle Maximum Isometric Force	0.8×nominal value	4×nominal value	S, G, T
λ_{ref}	Tendon Reference Strain	0.02	0.09	S, G, T, A
K_{sh}	Tendon Shape Factor	1	5	S, G, T, A
l_{sl} [cm]	Tendon Slack Length	0.7×nominal value	$\frac{\min(l_{\text{MTC}} - 0.5 l_{\text{opt}})}{\cos(\theta)}$	S, G, T

Table 3.4 summarizes these considerations. The bounds on tendon slack lengths and muscle F_{max} depend on the scaled subject-specific nominal values (introduced

in inputs Section 3.5.3). The subject-specific bounds calculated from the formulae using the literature values are listed in appendix Table 2. The last column shows the breakdown of 14 optimization variables across model elements S, G, T, A (Soleus, Gastrocnemius, Tibialis Anterior and Achilles tendon respectively).

Optimization Algorithm

Since the objective function is rather bumpy, a stochastic optimization method was deemed necessary to prevent the optimizer from getting trapped in local minima. The desired global minimum for this problem was implemented using a genetic algorithm (Direct Search Toolbox, MATLAB, Mathworks).

Table 3.5: Genetic Algorithm Optimization Settings

Option	Population Size	Elite Count	Crossover Fraction f_c	Initialize	Vectorized
Value	150	5	0.8	Nil	On
Value when Seeding	150	2	0.4	Seed Value	On

Most optimization runs were started from a random point (no seeding). The objective function was vectorized for speed so that many populations could be evaluated in parallel. The population size, elite count and crossover parameters were chosen to ensure diversity by preventing the optimization from getting stuck in specific infeasible or feasible regions. Some tradeoffs considered are outlined below:

1. Elite count specifies how many high fitness individuals are guaranteed survival to subsequent iterations. A low elite count would allow more diversity but would result in a very slow convergence. In contrast, a high elite count would speed up convergence, but would also make it more likely that the optimization gets stuck in infeasible regions early on and never hits a feasible space. The tradeoff was resolved by capping the elite count at about 3% of the population size.

2. The crossover fraction f_c determines the fraction of progeny that result from combinations of parameters within the parent population. A high crossover fraction prevents the optimization from getting stuck in feasible or infeasible region - since it allows mixing of the feasible and infeasible solutions in the population. But a high crossover fraction also limits diversity in evolution, as $f_m = 1 - f_c$ is the fraction of progeny resulting from random mutation-like factors. This tradeoff was resolved by capping the crossover fraction at 80%.

In rare cases, the algorithm was seeded with a randomly chosen feasible value to help it achieve feasibility faster. This value only restricts the initial population. To counter any restrictions on population diversity imposed by this seeding, the random mutation fraction was increased (by reducing the cross over fraction), and elite count was decreased (Table 3.5).

Handling Constraints

Many ways to handle non-linear constraints with genetic algorithms are actively discussed in the literature [31]. We chose to use the simple and efficient penalty method to enforce our non-linear constraint [32]. A static penalty of $1000 \cdot$Stance RMS Error was imposed when the modeled stance-phase ankle torque was off from the empirically obtained in vivo ankle torque by more than 1 standard deviation. The proportionality of the penalty with RMS Error between model and human torques drives the optimization down an RMS error gradient toward a feasible region. Mathematically, if there are n points over the stance phase:

$$cost = \begin{cases} C & \text{if constraint satisfied} \\ 1000\sqrt{\left(\frac{\sum_{i=1}^{i=n}(\tau_{mod}(i) - \tau_{bio}(i))^2}{n}\right)} & \text{otherwise} \end{cases} \tag{3.20}$$

The static penalties of 1000 worked well for our optimization most of the time. It allowed the algorithm to enter feasible regions, and leave unfavorable feasible regions for more favorable ones as and when needed. In the event that the optimization got stuck in a specific feasible region early on and did not randomly procreate infeasible individuals along the way, we helped it diversify using a population segregation approach outlined in [33]. In this approach, infeasible individuals within half the population suffer from a soft penalty of 10, while those within the other half are hit with a steeper penalty 100000. This, along with the crossing over feature of the genetic algorithm, allows the optimizer to leave energetically unfavorable feasible regions, and traverse through infeasible regions toward more favorable feasible regions as and when required.

3.5.6 Optimization Results

We summarize in this last section the results of the optimization procedure. Figure 3-8 shows convergence of a typical optimization run. There is no definite way of checking the optimization converges on a globally optimum solution. To test the accuracy of the minimum, we started a gradient descent[6] at the optimized values for one subject's data. This did not change results significantly suggesting that the genetic algorithm may have found a reasonably accurate minimum.

To improve speed and accuracy, the population diversity could be increased as this may encourage quick convergence with lower population size and/or generations. Further, feasible regions could be tightened by reducing standard deviation in ankle torque profiles by excluding outlier torque profiles. Finally, hardening the penalty in proportion to generation number can enforce the population to stay within feasible regions, prevent random time consuming searches and enable faster convergence as the optimization progresses. Of course, all these techniques trade-off the diversity and randomness which are deemed valuable to finding a global solution for our problem.

[6] using 'fmincon' in MATLAB

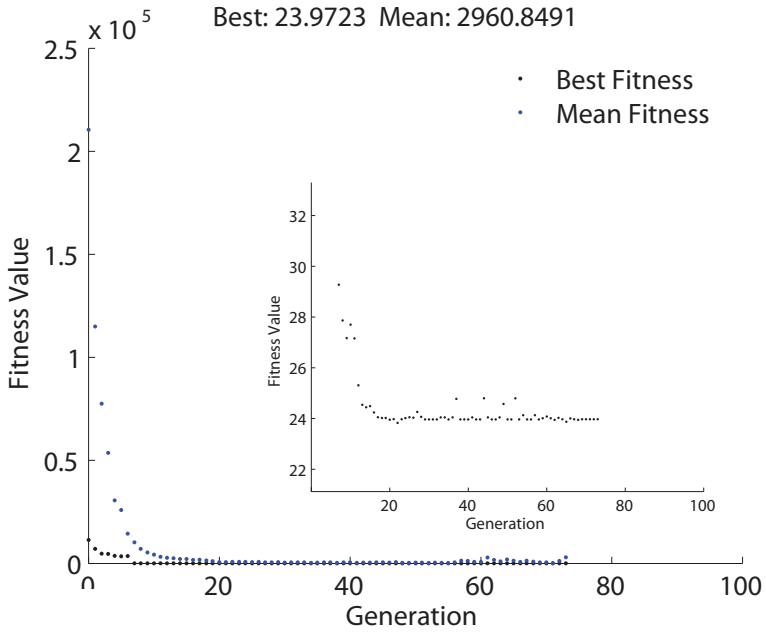

Figure 3-8: Convergence of the constrained genetic algorithm optimization. Search starts out in an infeasible space, and converges to a feasible region. Inset zooms in to feasible space.

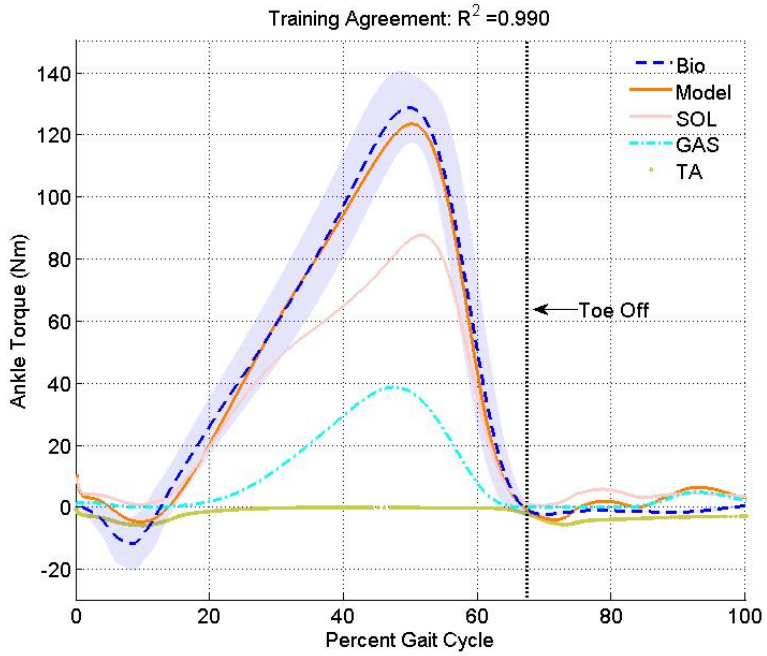

Figure 3-9: Agreement between trained model ankle torque and empirical ankle torque for a typical subject - on training data. The breakdown of different muscle contributions to the ankle torque is also displayed.

Model and empirical torques from this run are overlaid in Figure 3-9 to show that the constraint is satisfied. Table 3.6 displays the optimized morphological parameters and constraint agreement metrics for each subject. RMS Error torques were normal-

Table 3.6: Optimization Results

Subject	**JS**	**KE**	**RS**	**EJ***	**AS**
$\mathbf{F}_{\text{max, SOL}}[\mathbf{N}]$	5661	4520	4353	3974	7142
$\mathbf{F}_{\text{max, GAS}}[\mathbf{N}]$	1847	1801	1786	1520	1759
$\mathbf{F}_{\text{max, TA}}[\mathbf{N}]$	698	1243	1092	1245	2055
$\lambda_{\text{ref, SOL}}$	0.073	0.082	0.086	0.080	0.083
$\lambda_{\text{ref, GAS}}$	0.060	0.062	0.037	0.066	0.042
$\lambda_{\text{ref, TA}}$	0.057	0.054	0.037	0.030	0.058
$\lambda_{\text{ref, ACHI}}$	0.078	0.068	0.066	0.030	0.026
$\mathbf{K}_{\text{sh, SOL}}$	4.38	3.35	4.05	3.51	2.25
$\mathbf{K}_{\text{sh, GAS}}$	4.62	3.49	1.20	4.70	2.81
$\mathbf{K}_{\text{sh, TA}}$	1.90	2.14	3.92	4.00	1.12
$\mathbf{K}_{\text{sh, ACHI}}$	1.57	4.33	2.94	1.00	4.27
$\mathbf{l}_{\text{sl, SOL}}[\mathbf{cm}]$	27.9	25.8	26.5	21.8	25.8
$\mathbf{l}_{\text{sl, GAS}}[\mathbf{cm}]$	44.9	40.1	43.9	34.0	41.4
$\mathbf{l}_{\text{sl, TA}}[\mathbf{cm}]$	27.8	25.2	23.8	22.0	21.4
Stance R^2	0.990	0.971	0.994	0.996	0.972
$\mathbf{R^2}$	0.993	0.972	0.990	0.993	0.947

ized by BWLL or 'body-weight leg-length' calculated from values given in Table 3.1. For subject EJ(*), the optimization procedure had to be modified a little as the ankle torque from inverse dynamics had very high variability, allowing the optimizer to settle on parameter values and metabolic cost not representative of the mean profiles[7]

[7]High standard deviation allowed a large range in feasible values of $F_{\max}$. The optimizer settled in on the lower values within this range, corresponding to a feasible torque much lower than the mean. To overcome this, we (a) had the optimizer choose $F_{\max}$ to only influence feasibility and enforce a match with mean torque profile and (b) minimized $\sum_i \left[\frac{F_{\max,\text{nom,i}}}{\sum_i F_{\max,\text{nom,i}}} \text{ muscle costs unscaled by} F_{\max} \right]$ where $F_{\max,\text{nom,i}}$ were the nominal values for EJ in Table 1

There is some repeatability in ranges of the parameters across subjects. The high R^2 value indicates the efficacy of the optimization procedure, and shows that our method can find tendon parameters to explain the training data. With all parameters governing muscle state evolution identified, the system dynamics are fully determined. The muscle length and velocity profiles can be obtained from the Simulink solutions to the system with the optimized morphological parameters.

3.5.7 System ID Summary

To summarize this section, we focused on the overcoming the redundancy within the muscle-tendon complex to estimate muscle length and velocity. First, we defined the system dynamics, identified available inputs and framed the problem as a parameter ID problem. Then, we put forth a hypothesis based on known facts about locomotion energetics. We used it to develop an optimization technique for identification of key tendon morphological parameters influencing muscle length and velocity. Finally, we showed that the algorithm converges on a set of parameters within physiological ranges that capture the dynamic characteristics of the empirical data from our human subjects that was used for training. Henceforth in this thesis, "trained model for subject X" will be used to refer to the Simulink implementation of the muscle-tendon system, with dynamics defined by morphological parameters optimized for a training dataset from subject X.

3.6 Chapter Summary

This chapter summarized the many steps undertaken to use gross ankle gait data and obtain finer details regarding the neuromuscular and morphological functions governing ankle motion. All the techniques were based on information about biophysical mechanisms and/or statistical features in the data. As such, our framework is essentially a data-driven design optimization of the ankle musculo-skeletal structures for achieving human-like ankle dynamics in an energetically optimum manner. Our approach captures important features of both neural and morphological aspects of ankle motion during level ground walking. It also gives us estimates of muscle state evolution governed by these two interacting aspects. Before we can delve more into predictions about how these two aspects interact to move the ankle during gait, we must first validate the efficacy of the approach.

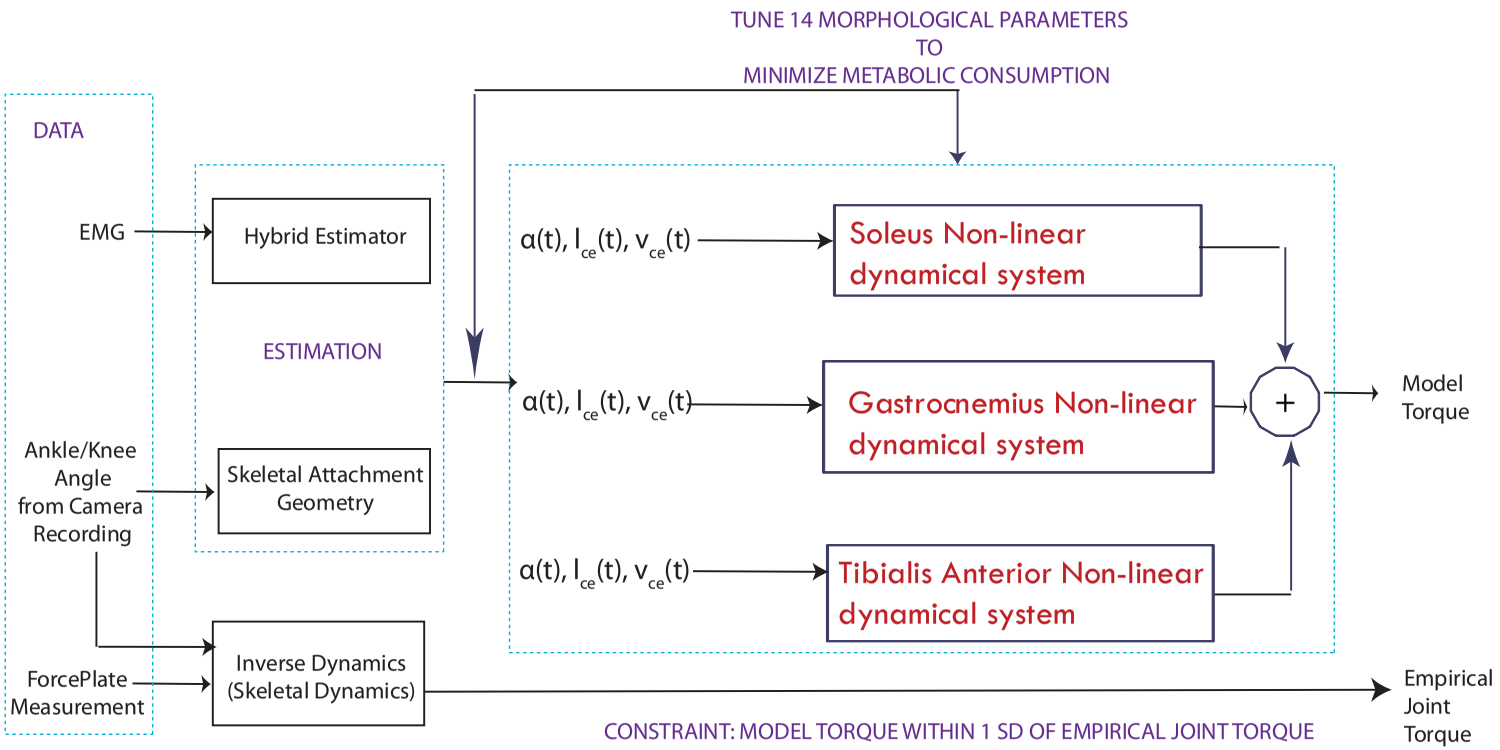

Figure 3-10: Summary of approach - from motion capture data to individual muscle states. We tuned tendon parameters to be able to obtain muscle states from data-driven estimators, with the constraint that the model dynamics matches the ankle dynamics.

Chapter 4

Efficacy of Approach

In this chapter, we analyze the efficacy of the technical components of the approach developed in Chapter 3. First we show the robustness of the EMG analysis technique, present failure modes and suggest ways to overcome them in future studies. Second we discuss the accuracy of the system ID technique, and present observations about the uniqueness and invariance of the optimized morphological parameters. Finally we cross-validate the overall modeling approach by showing efficacy on independent test data sets.

4.1 EMG-Activation Estimation Technique

This section will describe both successes and limitations of the hybrid biophysical-statistical approach proposed in Section 3.4.

4.1.1 Robustness

Two problems have prevented the use of EMG as a quantitative driving signal to mechanistic models:

1. The noisy nature of the signal and differences arising from day-to-day conditions and placement variations.

2. Difficulty in matching joint torque measurements in normal (non-isometric, non-maximal contraction) movements.

Here we point out the successes of our approach on these two fronts.

Firstly, the activation estimation technique is not easily led astray by random spikes in the EMG signal (Figure 4-1). A purely deterministic technique would not be able to accomplish this, and the Sanger statistical method becomes useful here. Further, the approach is quite robust. We tested how the algorithm responds to day-to-day variations in signals from the same subject, and saw that the resulting estimates looked quite repeatable. The approach also shows a lack of sensitivity to subject anatomy and works well across subjects with varying height, weight, size and definition of lower limb muscles. Finally, variations in electrode placement did not

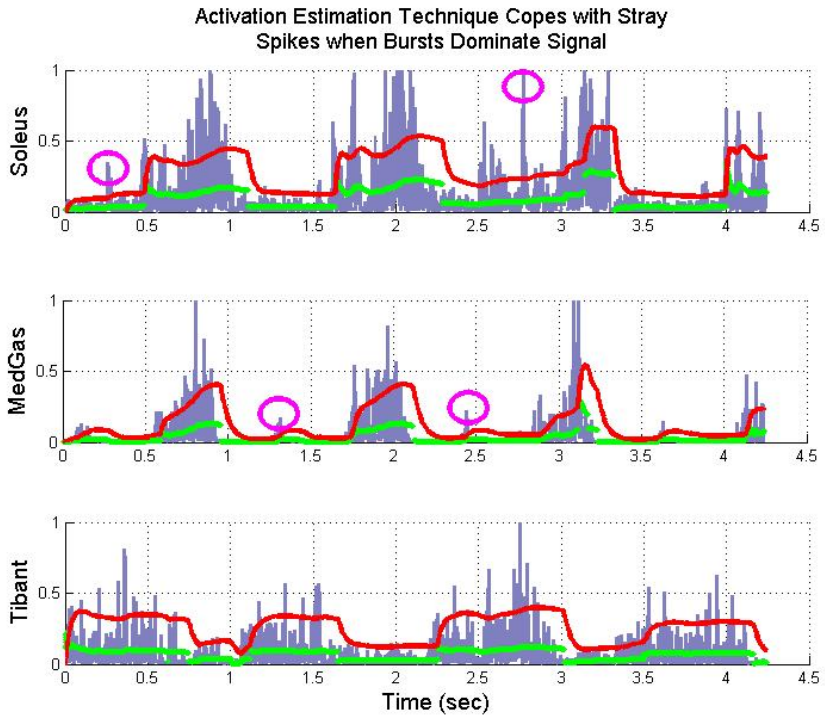

Figure 4-1: Activation estimates cope with stray spikes (circled) for all 3 ankle muscles.

much matter, as long as electrodes were placed approximately at the muscle belly, and oriented along the fibers.

The second success is evident from the optimization results in Section 3.5.6 which show that the estimates can drive a model to generate ankle torque matching human gait data. While this agreement does not validate the accuracy of the estimation procedure directly, it is one indicator of accuracy of the estimates. This indication is strengthened by other model predictions, which will be detailed in Chapter 5. A more direct validation would be possible if there were a way to measure EMG data along with the ground truth active state to check the estimator against. While this is hard to do *in vivo*, a setup reported by [34] helps make this possible *in vitro*, and this may help ascertain better the biophysical accuracy of our method.

4.1.2 Limitations

While the EMG method does well for most trials, it does not guarantee a good estimate for every trial. The averages presented and used in the system ID of Chapter 3, were only over trials where the EMG data seemed to fit the generally expected phasic trends. We left out extreme outliers that may have arisen from the unpredictability of the EMG measurement itself. An example of a failure mode is shown in Figure 4-2. The statistical part of the EMG algorithm fails when the data has a high noise floor. For instance, if the pre-processed EMG data has a high noise floor (greater than

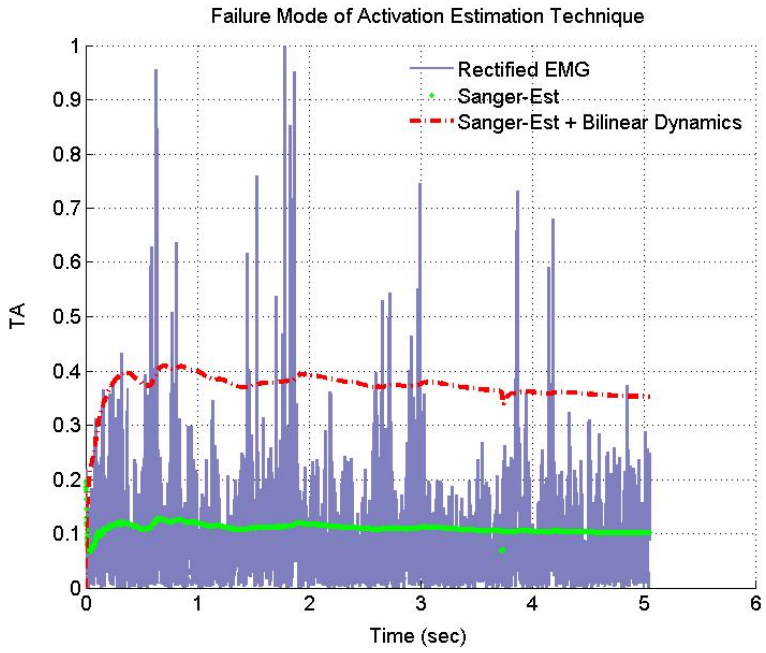

Figure 4-2: Main limitation of activation estimation algorithm - resulting in a non-phasic, aperiodic estimate when applied on non-bursty EMG data.

about 0.1), followed by a random spike-train like process, the statistical algorithm will struggle to rise up and go down. The challenge is to enable emergent adaptation of the algorithm to cases, like in the figure, where the phasic nature of the data is not completely clear from visual inspection. This problem is one of distinguishing between noise and signal bands that are both significantly stochastic, but may come from different distributions.

4.1.3 Future Work

The problem of distinguishing two stochastic processes can simply be thought of as a two-state model - noise state or signal state. The estimation algorithm would then have to detect changes in features like variance or zero crossing frequency. Change-point detection techniques take advantage of such features, and have been applied on EMG data [35]. But change-point techniques focus primarily on phasic features corresponding to state-transitions, and do not address the issue of estimating amplitude profiles. Detailed models of the two state dynamics would be necessary to define amplitude profiles of estimates. Given that we want to capture the biophysics, the best method would be to use Monte Carlo simulations on Sanger-like stochastic models that have state-dependent parameters.

This is conceptually similar to the problem - described in Section 3.4.2 - of using a stochastic model with time-varying jump and diffusion rates. The difference is that the source of the problem in this case is the noise band in the signal, and not the earlier need to capture history dependencies in the biophysics. Yet, the mathematical likeness may mean that both problems could be dealt with a similar technique. The

activation signal could be modeled as one that has a time varying rate and amplitude. The rate and amplitude could be parametric functions of both the instantaneous amplitude and frequency in the EMG data. The parameters defining these rate and amplitude functions, being time invariant, could be estimated with a particle filter approach.

4.2 System-ID Procedure

Having placed the estimates in practical context, we attempt to analyze the validity and shortcomings of the system ID procedure in this section. Since benchmark *in vivo* values of the morphological parameters are sparse and highly variable, we chose to test the efficacy using other metrics.

4.2.1 Speed Invariance

Since we are optimizing for invariant morphological parameters, the efficacy would be evident if we were to find the same parameters by applying our model identification framework on data of two distinct speeds.

For one subject, we applied the framework on data from two sets of trials where the subject was asked to target speeds of 1.25 m/s and 1.50 m/s respectively. The results are reported in the Table 4.1. We see low percentage variations between optimized parameters obtained from training the model on different speed walking data. Further we see good agreement between model and ankle torque, showing that the constraint has been fulfilled in both cases.

Table 4.1: Invariance of Morphological Parameters Across Speed

% Variation	$\mathbf{F}_{\max}$	λ_{ref}	$\mathbf{K}_{\text{sh}}$	$\mathbf{l}_{\text{sl}}$	**Stiffness**
SOL	−1.0	−3.5	−52.1	−4.1	11.7
GAS	−0.91	5.3	11.5	−0.18	8.9
ACHI		−7.0	7.0		6.1
Agreement	**Stance** R^2	R^2	**Stance RMS Error [N]**	**RMS Error[N]**	
KE125	0.971	0.972	7.28	7.28	
KE150	0.928	0.922	9.21	11.2	

A note on KE150 training: The feasibility condition was enforced only for times when ankle torque was positive, as one standard deviation of dorsiflexor torque was slightly off from all model predictions. We believe this happened because faster

walking demands faster rise of ankle torque, that may have demanded smaller plantar flexor muscles to be on earlier, and a different dorsiflexor action to ensure these muscles did not over extend the ankle. Since the other muscles were not modeled or measured in our study, we had problems in fitting the early stance dorsiflexor constraint. The system ID for the plantar flexor muscles is consistent with that applied to the 1.25 m/s data. Due to this difference, the table only displays comparisons for the plantar flexor muscles.

Most optimized morphological parameters have very small variations between the two speeds. This lends credence to the approach. The table also shows that the K_{sh} parameters have wide variations across speed, but the resulting stiffness values (calculated as the linear slope of the high force regions of the tendon force-length relation) are conserved more than the K_{sh} values are. This suggests that the optimizer may be operating for a unique solution in tendon stiffness space instead of in individual tendon parameter space. A future method that adapts our technique to capture individual trial to trial variability would help understand better what functions of these parameters are conserved across steps. These observations raise the question of uniqueness of the optimizer solution, which is explored in detail in the next section.

4.2.2 Uniqueness of Optimizer Solution

To understand better the uniqueness of the optimizer solution, we repeated the system ID runs on self-selected speed data for one of our subjects (JS). The results across five separate runs on the same data are documented in Table 4.2 and Figure 4-3.

Table 4.2: Uniqueness of Solution: Soleus Tendon Parameter Trends

Run #	**1**	**2**	**3**	**4**	**5**	**Average**	**Standard Deviation**
$F_{\textbf{max,SOL}}$ **[N]**	5026	7642	5716	6282	5801	6093	975
$l_{\textbf{sl,SOL}}$ **[cm]**	28.2	27.6	28.3	28.9	28.5	28.3	0.48
$\lambda_{\textbf{ref,SOL}}$	0.066	0.079	0.069	0.055	0.070	0.068	0.009
$K_{\textbf{sh,SOL}}$	4.08	4.05	4.64	3.66	4.21	4.13	0.35

The question is whether the unique values of these morphological parameters came from the imposition of the energetic minimum, or if the repeatability was imposed by the feasibility constraint alone. By hardening and relaxing the feasibility constraint, and checking changes in the optimized parameters, it was found that the slack lengths were mainly determined by the feasibility constraint. This is reasonable because the ankle torque data dictates when the muscles can be on and off. In other words, the data tells us when the tendon had to be stretched beyond slack for force generation. The Soleus $F_{\text{max}}, K_{\text{sh}}$ and λ_{ref} parameters, on the other hand, depended on the metabolic cost for their repeatability. This lends credence to the driving hypothesis

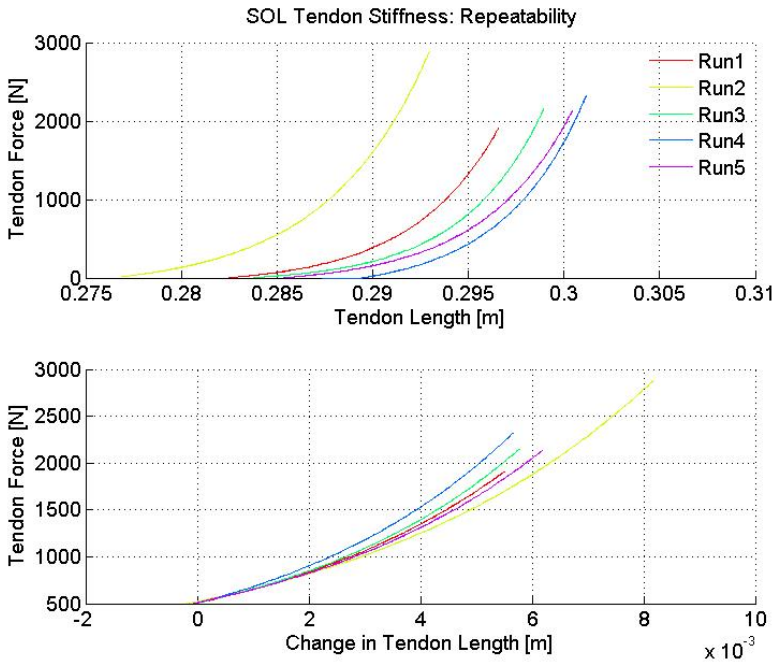

Figure 4-3: Soleus tendon force-length curves. Soleus stiffness is calculated as derivative of the higher force regions of the force-length relation where linearity is more likely. Like the soleus parameters, is very repeatable across runs 0.290 ± 0.028 MN/m. The lower graph shows all the curves normalized to the same scale for easy comparison.

that the morphological parameters (along with neural control) are tuned uniquely for minimum metabolic cost of muscle operation during walking.

To probe further the uniqueness of parameter values obtained, we provide in Table 4.3 optimized parameters for other muscle-tendon units from the five repeat runs on subject JS discussed earlier.

The average and standard deviation values across five runs give a sense of the variability in optimized parameters. The values for most parameters in Table 4.3 have greater variability than the Soleus parameters. The relevant question here is whether this variability is because our hypothesis only imposes uniqueness of Soleus parameters, or if the lack of repeatability arises from a technical limitation of the optimization. We believe the latter case is more likely. This is because the parameters having high variability correspond to muscles that have small contributions to the optimized cost - in contrast with the Soleus which dominated the metabolic cost for this subject[1]. Mathematically, if

$$[x_1, x_2] = \arg\min(C_1(x_1) + C_2(x_2)) \text{ and } C_1 \gg C_2 \tag{4.1}$$

the optimization will be driven mainly by x_1 not x_2. This may appear contradictory with the slack length repeatability (dark shaded cells) seen for all muscles - even the Tibialis Anterior which has very low cost contribution. But it must be noted that

[1]Soleus does not dominate cost for all subjects

Table 4.3: Uniqueness of Solution: Other Muscle-Tendon Units?

Run #	**1**	**2**	**3**	**4**	**5**	**Average**	**Standard Deviation**
$F_{\mathbf{max,GAS}}$ **[N]**	2322	1747	1858	2580	1766	2054	376
$l_{\mathbf{sl,GAS}}$ **[cm]**	45.9	47.4	44.8	47.2	44.8	46.0	1.3
$\lambda_{\mathbf{ref,GAS}}$	0.055	0.053	0.041	0.027	0.031	0.041	0.013
$K_{\mathbf{sh,GAS}}$	4.15	4.61	2.27	4.26	3.85	3.83	0.91
$F_{\mathbf{max,TA}}$ **[N]**	1465	1525	1504	1548	1480	1504	34
$l_{\mathbf{sl,TA}}$ **[cm]**	28.7	28.2	28.6	29.2	28.8	28.7	0.35
$\lambda_{\mathbf{ref,TA}}$	0.023	0.023	0.033	0.065	0.038	0.037	0.017
$K_{\mathbf{sh,TA}}$	4.93	3.45	1.62	2.00	3.39	3.08	1.32

slack lengths repeat due to the constraint not the cost, and the constraint applies equally to all muscles. The constraint-induced repeatability is also seen in the $F_{\max}$ values (dark shaded cell) for low-force muscles like the Tibialis Anterior.

To overcome the technical limitation causing variations in some of the morphological parameter results, each muscle could be optimized separately in a step-by-step fashion. The key would be to consider the net ankle torque matching constraint at each step, while only optimizing for single element cost contributions, and then using those optimized values to constrain the solutions of subsequent elements.

Finally, we discuss the effect of the optimization on parameters of passive structures (like Achilles tendon, and in more elaborate models ligaments), which do not contribute directly to the metabolic cost.

Table 4.4: Uniqueness of Solution - Achilles Tendon Parameter Trends

Run #	**1**	**2**	**3**	**4**	**5**	**Average**	**Standard Deviation**
$\lambda_{\mathbf{ref,ACHI}}$	0.046	0.029	0.060	0.032	0.036	0.041	0.013
$K_{\mathbf{sh,ACHI}}$	3.63	1.87	4.61	1.34	3.33	2.96	1.33
$k_{\mathbf{ACHI}}$ **[MN/m]**	4.87	7.19	4.26	6.78	5.92	5.81	1.24

The Achilles tendon parameters are highly variable. The key conserved trend is that the Achilles tendon is much stiffer than other tendons. We found that this

high stiffness trend is primarily imposed by feasibility constraints[2]. The high stiffness is consistent with literature reports showing that the Achilles is among the stiffest tendons in the body [36]. However, the optimization often converges on stiffness values larger than cadaver reports. This could be because the mathematical bounds set in the optimization do not necessarily reflect space and material properties constraining the physical bounds. Discrepancies could also arise from the stiffness calculation itself - which is a linear approximation of the changing slope of the tendon force-length relation. Regardless of actual values, it is meaningful that the feasibility constraint imposes a high stiffness on the Achilles tendon, and insights gained from this trend are discussed in Chapter 5.

4.3 Cross-Validation

Having discussed the efficacy and limitations in the estimation and system ID parts, we now evaluate the predictive power of the overall approach. A good measure of this is the performance of the entire framework on independent test datasets. To test this, we performed cross-validation trials that test the trained model for each subject, with mutually exclusive testing datasets from the same subject. We split all gait data for a given subject into training and testing categories. So for a given input variable, its train data and test data were from mutually exclusive sets of gait cycles.

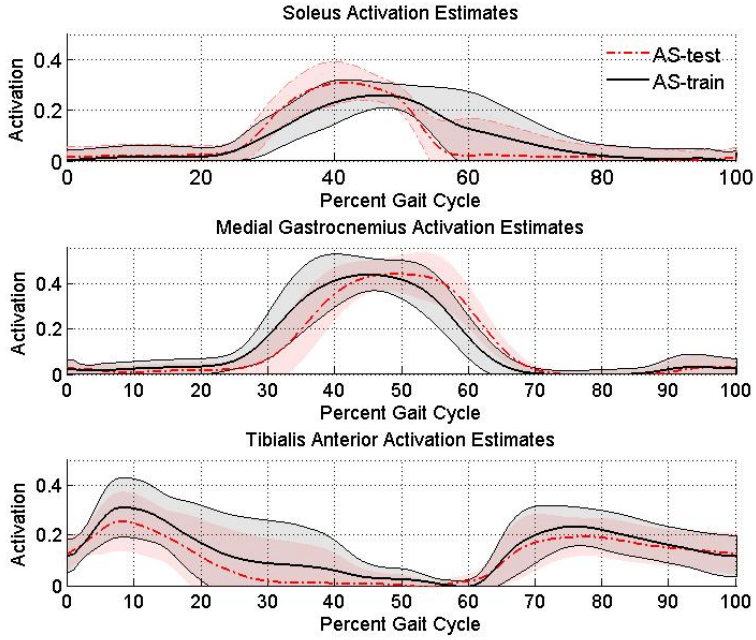

Figure 4-4: Comparison of training and testing active-state estimates since these were more variable than other model inputs.

[2]from experiments similar to those described earlier for slack lengths

Figure 4-4 shows an example of differences in the training data used to identify the system, and the testing data used to validate the system ID. Testing-training deviations in muscle-tendon length estimates are low due to the phasic patterns governing gait data. Figure 4-5 and Table 4.5 summarize the cross-validation results.

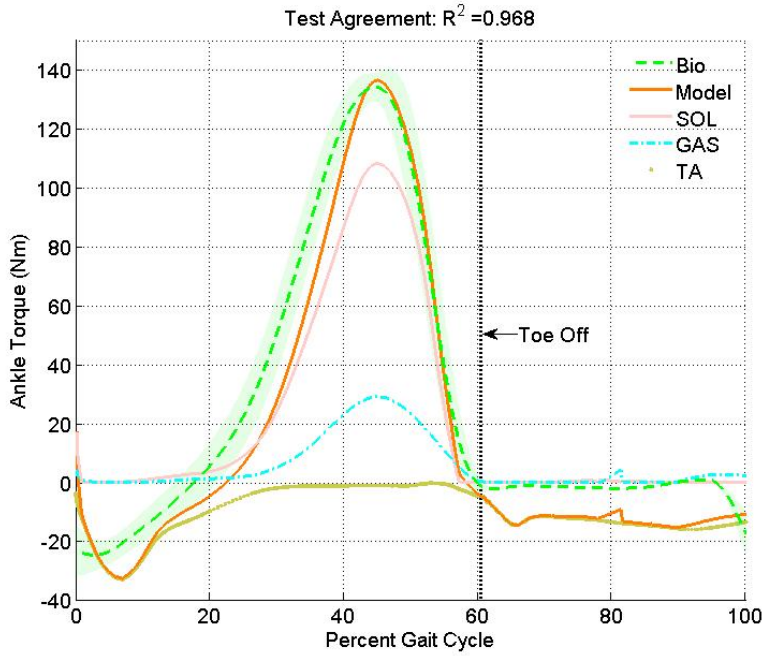

Figure 4-5: Agreement of ankle torque from an independently trained model with test data for a typical subject. The individual muscle contributions to ankle torque are also displayed.

Table 4.5: Cross-Validation of Model: Agreement with Test Data

Subject	**Stance R^2**	R^2	**Stance RMS Error[Nm]**	**RMS Error [Nm]**	**Stance RMS Error [BWLL]**	**RMS Error [BWLL]**
JS	0.991	0.994	4.23	3.86	0.050	0.046
KE	0.931	0.940	11.6	10.9	0.161	0.151
RS	0.955	0.950	8.93	7.67	0.118	0.101
EJ	0.982	0.982	4.70	4.41	0.075	0.070
AS	0.968	0.945	10.1	10.6	0.120	0.126
Average	0.965	0.962			0.105	0.099
KE150	0.916	0.901	14.9	13.3	0.206	0.184

The table summarizes metrics quantifying agreement of ankle torque from an independently trained model with test data. Even though the model was trained only till stance end, the full gait cycle agreement metrics are as good as the stance agreement metrics. Since the R^2 value is consistently high, the RMS Error is also provided to quantify match in physical units. For one subject, agreement with test data from a faster walking trial was evaluated. The results of this faster speed are listed as KE150 metrics. They are obtained by training the model with KE 1.25 m/s data, and then cross-testing it on KE 1.50 m/s data. The good agreement even with faster speed testing data shows the model is predictive outside of speeds for which it is trained.

4.4 Chapter Summary

In this chapter, we discussed steps taken to analyze the success and limitations of our (a) estimation technique and (b) system ID methods in view of the goals underlying their development. For the former case, we showed that the approach is robust to noise and electrode placement variations. For the latter case, we showed the power of the approach to converge on unique solutions for morphological parameters. Overall, we showed that there is good model-empirical ankle torque agreement and high predictive power in cross-validation trials. While this validates the hypothesis, techniques and simplifications underlying our framework, it is also to be expected since the model was trained to produce human-like ankle torque during walking. The real value of a model stems from its ability to predict aspects that were (a) not constrained in model identification and (b) not evident from simple functions of the inputs. Examples of such predictions include muscle length/velocity profiles, and insights into neural and morphological interactions governing muscle action during walking. These predictions are the topic of the next chapter.

Chapter 5

Results and Discussion

This chapter is about the value of the framework developed and validated in Chapters 3-4, in providing non-apparent insights into muscle action, neural control and leg structure. First, we present model predictions of ankle plantar flexor muscle length and velocity profiles. Then we analyze the estimated muscle states to extract insights about the interplay between neural control and leg structure that we set out to understand. Specifically we discuss the influence of structure, control and the interactions between the two on (a) the distinct roles of the ankle plantar flexor muscles, and (b) metrics relating to the performance of these muscles. We end with a summary of the key contributions to the gait modeling literature, with reference to our goal of resolving neural-structural interactions.

5.1 Muscle Length and Velocity

Muscle length and velocity are central to understanding interactions between tendon structures and the neural controller. This is because length and velocity are (a) influenced by tendon morphology due to muscle-tendon dynamics and (b) fed back to the spinal cord through muscle spindle sensors to excite neural reflex pathways.

While there have been reports of ultrasound scans of human ankle plantar flexor length [37, 38, 39], there are no reports of model-based estimates of these profiles. This is probably due to the complex, non-linear and history dependent nature of the biophysics governing their evolution. In this section, we present our model-based estimates of muscle length velocity. Since the model was trained for minimum ankle metabolic cost, and this cost is dominated by the stance-phase activity of the powerful Soleus and Gastrocnemius muscles, we only discuss predictions for these two muscles. We compare our length estimates with empirical data reported in the literature, and discuss some observations regarding trends in the length and velocity profiles.

All estimates presented were evaluated by applying subjects' testing dataset(s) (Section 4.3) on their trained model(s) (Section 3.5.7). Since it only makes sense to evaluate muscle state when muscles are 'on' and working, all figures are presented for stance phase only. The variation in estimated profiles was calculated by propagating kinematic and kinetic variability - which are dominated by variations in muscle-tendon

length and activation estimates respectively[1].

5.1.1 Length

Muscle length and tendon length estimates were obtained from the solution to the system equations parameterized by optimization results. Figures 5-1 and 5-2 show that the model-based Soleus length predictions agree qualitatively with *in vivo* evidence.

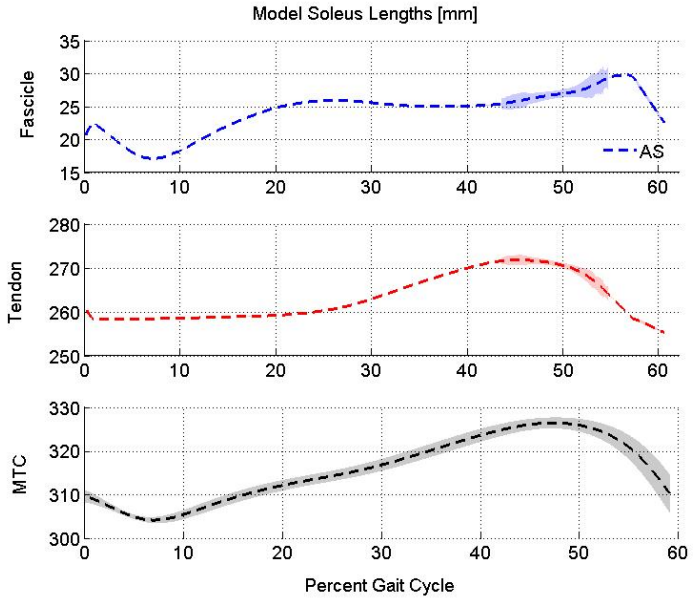

Figure 5-1: Model Predictions of Soleus muscle (Fascicle), tendon (TT) and muscle-tendon unit length (MTU). Standard deviations are propagated from those of estimates. After early stance, muscle lengthens till the end of single stance and shortens till toe off.

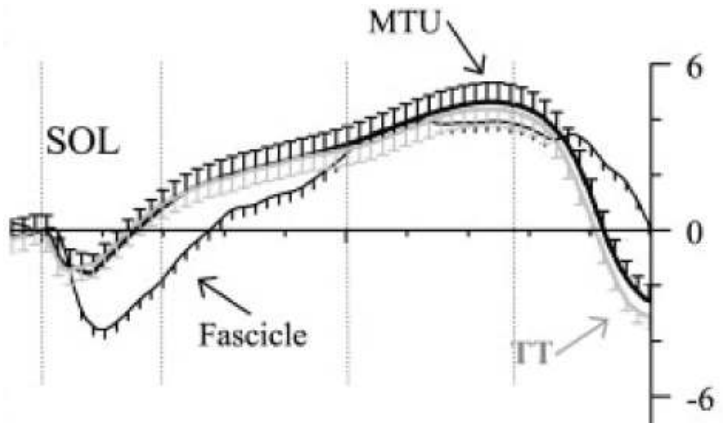

Figure 5-2: In vivo empirical measurement of Soleus lengths provided for comparison. Source [37]. Y-axis is percent change from heel strike.

[1]an error propagation analysis considering correlations of different errors will be better

It is clear that there is high quantitative agreement between model and *in vivo* tendon and muscle-tendon lengths. It is striking that this does not translate to a high quantitative agreement between model and *in vivo* muscle lengths since muscle length is essentially:

$$l_{\mathrm{CE}} = (l_{\mathrm{MTC}} - l_{\mathrm{SE}})/\cos(\theta) \quad \theta = \text{pennation angle} \tag{5.1}$$

This leads us to believe that the quantitative differences in muscle length may be because of inconsistencies between the model's geometry and the complex *in vivo* geometry. There are a few sources for discrepancy:

1. Differences between dimensions of the subject AS and the subject studied in [37]

2. Differences in Achilles tendon geometry arising from our lumped element model, and the fact that we set the slack length at $3\,\mathrm{cm}$[2].

3. Differences in pennation angle - we set constant pennation angles in our model, while there are changes in this angle during movement as the muscle contracts and surrounding structures move.

Further, the peak stretch/contraction magnitudes reported in [37] are small (within 6-8%). Literature reports suggest that it is reasonable for the Soleus muscle to have high magnitudes of stretch and contraction during walking as the muscle fibers are short relative to the muscle moment arm [29]. The numbers in our model follow this latter trend.

The Gastrocnemius muscle length estimates for the same subject look quite different from the Soleus length estimates - even though the two muscles are known to act synergistically in gait. Figure 5-3 and 5-4 show the Gastrocnemius estimates, and the *in vivo* evidence from [37] respectively.

Comparing figures 5-1 and 5-3, we observe that the Soleus has higher length changes than the Gastrocnemius during most of stance. From Figures 5-3 and 5-4, we also see that the model-based Gastrocnemius length predictions agree qualitatively with *in vivo* evidence - for muscle, tendon and the muscle-tendon unit. The model reliably captures the key features of (a) early stance shortening and lengthening, (b) stance-phase isometric action and (c) the shortening right before toe-off.

Again, there is a disparity in quantitative metrics such as peak muscle shortening with respect to heel strike. The data in [37] predicts a value of 10%, while our model predicts 27%.

[2] we fixed this as it is a geometric feature, with no influence on any feasible metabolic costs

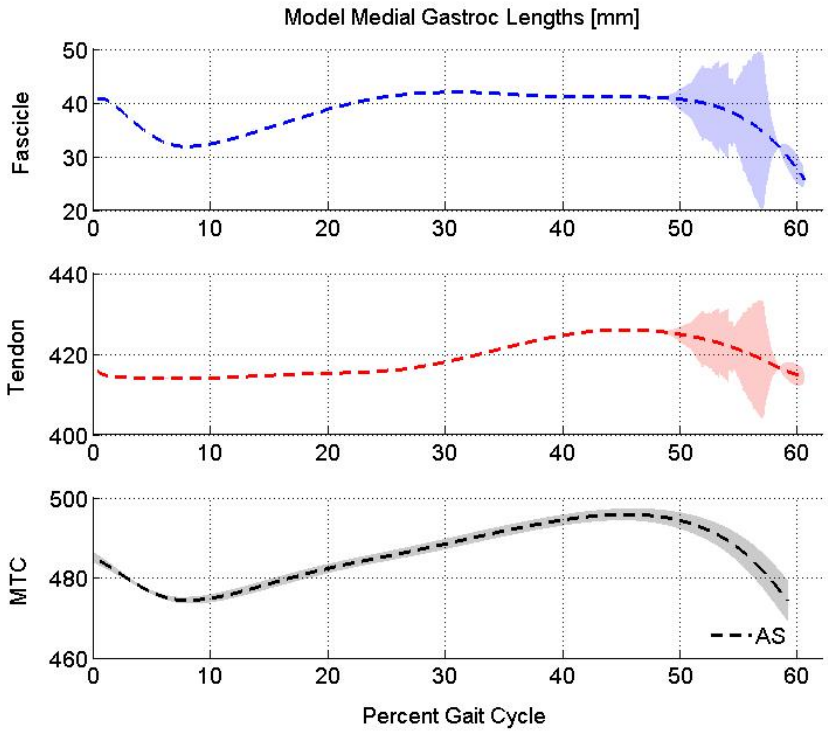

Figure 5-3: Model Predictions of Gastrocnemius muscle (Fascicle), tendon (TT) and muscle-tendon unit length (MTU).

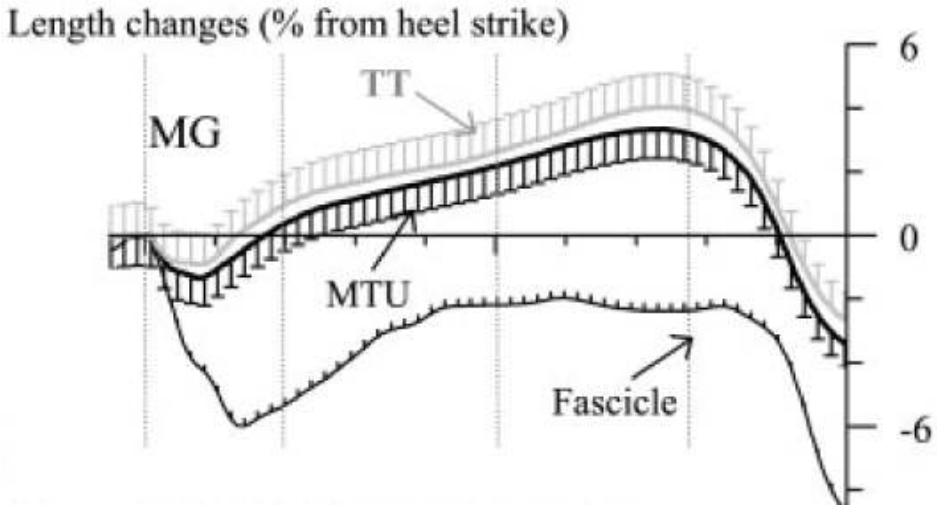

Figure 5-4: In vivo empirical measurement of Gastrocnemius lengths provided for comparison. Source [37]. Y-axis is percent change from heel strike

While this may also be due to geometric discrepancies similar to those mentioned earlier for the Soleus, it may also be due to subject-subject differences and variations in the in vivo measurement itself. Figures 5-5 and 5-6 compare model predictions for a different subject with a different *in vivo* measure [38] to illustrate this latter

possibility.

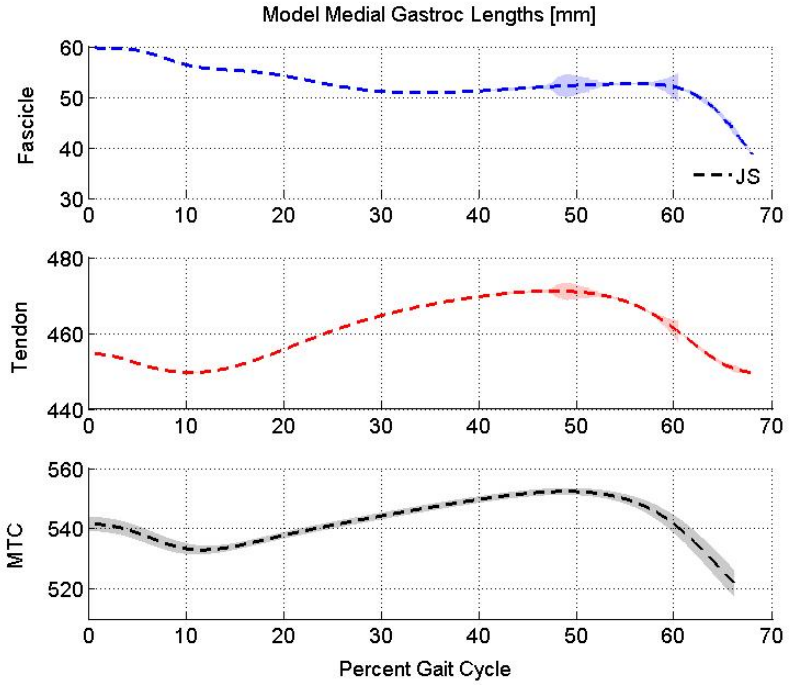

Figure 5-5: Model Predictions of Gastrocnemius muscle (Fascicle), tendon (TT) and muscle-tendon unit length (MTU) for subject JS. The fascicle length is largely isometric between $30 - 60$ %GC.

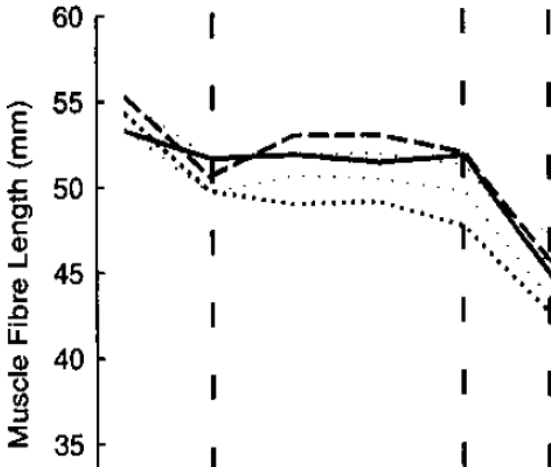

Figure 5-6: Lichtwark *in vivo* empirical measurement of Gastrocnemius lengths provided for comparison. The different curves are measurements at three ultrasound sites (distal is dotted, medial is solid and proximal is dashed. Source [38].

A comparison of Figures 5-5 and 5-6 reveals that the model estimate is quantitatively consistent with the *in vivo* measure, in addition to the qualitative agreement seen from Figures 5-3 and 5-4. This is due to differences between Lichtwark [38] and Ishikawa [37]) ultrasound scans respectively.

The Lichtwark scan reports a peak shortening of around 20%, as opposed to the Ishikawa scan where the peak is below 10%. The former looks closer to our model estimates both for subjects JS and AS. Further, the early stance muscle action in the Lichtwark scan is different from the Ishikawa early stance action. Both these different trends are captured by the model, for subjects JS and AS respectively.

Thus empirical measurements show a disparity in peak shortening and early stance action for the Gastrocnemius muscle. Our model suggests that this disparity may be due to differences between individual walking data. Out of the model-based Gastrocnemius length estimates for 5 subjects: 2 show the trends in Ishikawa, 2 show the trends in Lichtwark, while 1 is an outlier. The outlier subject was a professional athlete, had ACL injuries and had a large standard deviation in his ankle torque data (which could have impacted the training procedure).

Regardless of these differences in early stance action and peak shortening, the stance phase isometric action is a conserved feature - in both the *in vivo* estimates and in our model predictions for subjects AS and JS.

5.1.2 Velocity

The conserved features, such as isometric action, are easier to see in estimated muscle velocity profiles. Further, muscle velocity has been a corner-stone of many empirical studies vital to understanding muscle operation [12, 13]. This makes velocity a valuable source of information for quantifying what performance levels are demanded of muscle by the neural controller and the movement apparatus.

Muscle velocity was calculated as a smoothed derivative of the muscle length estimates obtained from the model above. The length standard deviation l_{sd} was propagated with the partial derivative formula to find the velocity standard deviation v_{sd}:

$$v_{\text{sd}}(t) = \frac{l_{sd}}{(t - t_0) \cdot v_{\max} \cdot l_{\text{opt}}} \tag{5.2}$$

Figures 5-7 and 5-8 show the Soleus and Gastrocnemius velocity estimates respectively. It appears that both plantar flexors are operating at almost 0 velocities for most of stance. There are small lengthening and shortening phases but the muscles hardly ever operate at high velocities. The Soleus muscle length changes a lot but given that the Soleus fibers are so short and that the muscle is slow, the rate of length change is tiny. This makes sense because these muscles deliver high forces and high powers to propel the body forward during stance, and the muscle dynamics tells us that high velocity operation would make this impossible. Further, the metabolic cost of near-isometric muscle operation is very low (Figure 3-7). So the trends in the velocity profiles indicate that muscles are operating to produce high forces at low cost for most of stance phase.

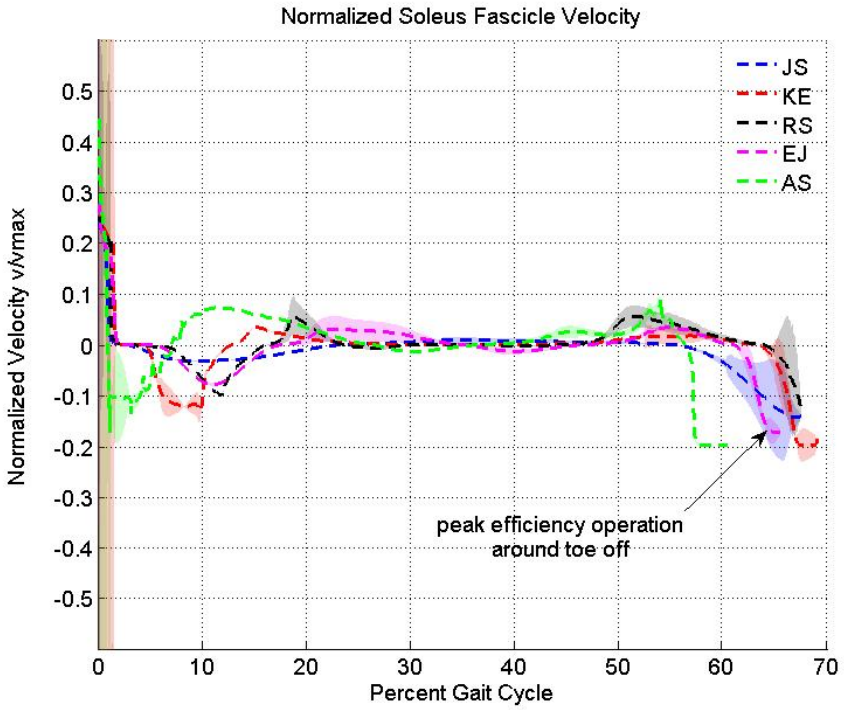

Figure 5-7: Model predictions of Soleus muscle (Fascicle) velocity for different subjects.

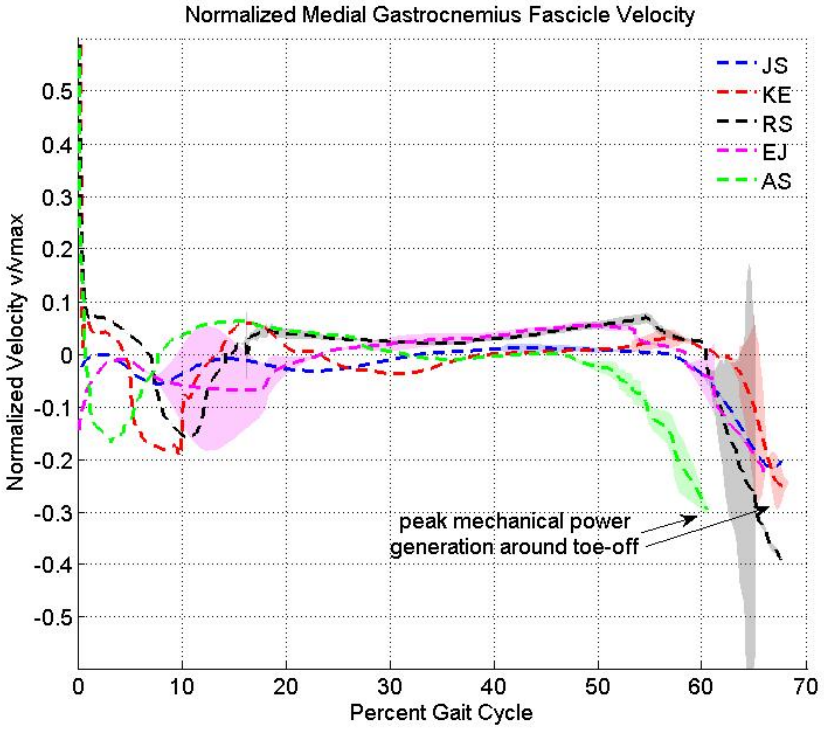

Figure 5-8: Model Predictions of Gastrocnemius muscle (Fascicle) velocity for different subjects.

The near-isometric action in stance and the end of stance shortening are common features of the operation of both Soleus and Gastrocnemius muscles. However, there is a key difference in the action of these two muscles during peak shortening (highly negative velocity) just before toe-off. The Soleus is operating at a peak velocity of $0.15v_{\max} - 0.20v_{\max}$, while the Gastrocnemius operates at a peak velocity of $0.28v_{\max} - 0.35v_{\max}$. The significance of these numbers is apparent from the results of the *in vitro* studies reported in [40]. This paper found that muscle efficiency peaks at 0.44 when $\frac{F_{\text{CE}}}{F_{\max}} = 0.45 - 0.50$ or equivalently $v \approx 0.17{v_{max}}^3$, while muscle mechanical power peaks around $v = 0.3v_{\max}$. Further, at velocity of $0.3v_{\max}$, the efficiency is about 0.40 - only less than maximum efficiency by $3 - 5\%$. Thus the model suggests that the Soleus operates around peak efficiency just before toe-off, while the Gastrocnemius operates synergistically in its peak mechanical power regime.

5.1.3 Section Summary

In this section, we presented ankle plantar flexor length and velocity estimates, and discussed them in light of *in vivo* and *in vitro* empirical measures respectively. We then compared the two muscles in view of their length profiles and operating regimes. The commonalities and differences found suggest that a detailed discussion of the roles and performance of the two muscles may help understand better their co-operation in gait.

5.2 Roles of Soleus and Gastrocnemius Muscles

The above observations regarding distinct roles for the plantar flexor muscles are consistent with several structural and neural features distinguishing their actions. In this section, we reflect on some of these features, and use the model to obtain a quantitative metric of role division between the two muscles.

5.2.1 Structure

Histological features of the plantar flexor muscles support the observation about the distinct peak efficiency-peak power operating regimes of the Soleus and Gastrocnemius at end of stance. Soleus muscle fiber composition estimates suggest that it is a muscle dominated by slow oxidative fibers [20]. Thus it can function steadily with low metabolic consumption, contributing to its ability to work at high efficiency. The Gastrocnemius, on the other hand, is a faster muscle and has more anaerobic fibers [41]. This means that it can activate faster than the Soleus, and generate mechanical work quickly which may be the reason for its high mechanical power operation [20, 25]. Being able to generate high power via quick increases in activation may mean that the Gastrocnemius can operate isometrically as it does not need to work

[3] for a wide range of muscle lengths

at high shortening velocity for quick power generation. This isometric operation is more economical too.

The differences in articulation of the two muscles may also be contributing to this role division. It is acknowledged in the literature that the Soleus is a mono-articular steady energy source to help maintain vertical position and power forward propulsion [10]. In contrast, the Gastrocnemius is a biarticular muscle spanning both knee and ankle. Therefore it has a key role as a burst energy source both at the knee and ankle - to help initiate the leg into swing phase [10].

5.2.2 Control

The same observation about operating regimes can be discussed in view of neural control or effectively the muscle activation estimates (Figure 3-5). The activation estimates tell us that the Soleus is the steady, basal muscle. It turns on first, right around when the ankle joint starts to extend, and stays on till end of stance. The Gastrocnemius on the other hand, is turned on after the Soleus, just in time so that it can help pump up plantar flexor power - making it the power muscle. This theory also has support from the fact that the Gastrocnemius is much more active than the Soleus during faster walking and running.

5.2.3 Structure and Control

While there are trends in the structural and control features, there is an interesting trend in the roles of the two muscles that is not independently due to either factor, but may be arising from co-operation of the two aspects.

By applying our trained model on data for all five subjects, we obtained the ratios of peak torques delivered by the Soleus and Gastrocnemius. As shown in table 5.1, this ratio (SOL to GAS) is quite consistently around $2:1$ (in one subject's case it was $5:2$, but that subject was distinct because he was tall and stocky).

Table 5.1: Plantar Flexor Ankle Moment Breakdown

Subject	JS	KE	RS	EJ	AS	Average	Standard Deviation
Ratio of Peak Forces	2.26	1.94	2.28	2.11	2.56	2.23	0.230
Ratio of Metabolic Costs	0.726	2.47	0.841	0.764	1.65	1.29	0.761

The trend is significant since the ratios of the optimized $F_{\max}$ of these two muscles varies from 2 to 4 (table 3.6). This suggests that morphological features alone would fail to explain this trend in the roles of the individual muscles. Further the ratios in peak activation of Soleus and Gastrocnemius varies across subjects too (Figure 3-5)

- suggesting that neural control alone is not responsible for this trend. While the ratios of the metabolic costs displayed in the above table are quite variable too, we know that the optimized solutions corresponded to a minimum of total plantar flexor metabolic cost (approximately since the Tibialis Anterior contribution is small).

Whether this ratio is a cause or result of enforcing that minimum metabolic cost is unclear. But the optimizer's breakdown of net ankle torque required by the constraint of matching the empirical torque may be understood as follows:

- Given the neural activation and muscle tendon length estimates, there is a dynamical limitation on the maximum Soleus torque across all possible Soleus tendon parameters. The Gastrocnemius now has to compensate for the remaining ankle torque. So this ratio is known.
- But maybe it is too expensive for the Soleus to generate that maximum torque, and it may be cheaper for the Gastrocnemius to generate a little more. Then the tendon parameters will be adjusted accordingly.
- And more adjusting of tendon parameters will follow - till convergence to a minimum which may coincide with the peak torque ratios in the table.

How this peak ratio is maintained in the body so consistently is an open question, which could be explored in a future study or through a clever empirical approach.

5.2.4 Section Summary

This section discussed the distinct roles of the Soleus and Gastrocnemius muscles in view of their structure (composition and articulation) and neural control. We presented a conserved metric suggesting quantitative breakdown of the torque-generating roles of the two muscles, and suggested that it may be correlated with a minimum net plantar flexor metabolic consumption. With the roles designated, we can now study features impacting metabolic and mechanical performance of the plantar flexors.

5.3 Ankle Plantar Flexor Performance

In this section, we discuss predictions regarding features of leg structure (tendon stiffness and slack length) and neural control that could impact muscle energetics. We then show how these features may be helping these powerful muscles perform with high efficiency by evaluating the net plantar flexor efficiency using our model.

5.3.1 Structure - Conserved Morphological Features

Tendon Compliance

Our system ID procedure found low Soleus and Gastrocnemius tendon stiffness and a high stiffness for the common Achilles tendon connecting the two plantar flexor muscles to the heel.

Table 5.2: Stiffness of Different Tendons in the Model

Subject	JS	KE	RS	EJ	AS
kSOL [MN/m]	0.291	0.214	0.245	0.337	0.228
kGAS [MN/m]	0.103	0.096	0.103	0.150	0.111
kTA [MN/m]	0.029	0.062	0.099	0.114	0.125
kACHI [MN/m]	2.62	3.97	3.10	3.26	10.6

A compliant tendon in a muscle-tendon unit allows economic force generation. A compliant tendon allows the muscle to operate at low velocities v_{m} for a given load velocity v_{MTC} [42]. This is clear from the following equation relating muscle velocity to tendon and muscle stiffness (k_{t} and k_{m}), and load velocity:

$$v_{\mathrm{m}} = \frac{k_{\mathrm{t}}}{(k_{\mathrm{t}} + k_{\mathrm{m}})} \frac{v_{\mathrm{MTC}}}{\cos(\alpha)} \tag{5.3}$$

For a given v_{MTC}, v_{m} is low when k_{t} is low i.e. when tendon is compliant. As discussed in Section 5.1.2, lower velocity operation is metabolically favorable.

But one may argue that the stiff Achilles tendon common spring could compromise this metabolic advantage of tendon compliance. On average the Achilles tendon is about an order of magnitude stiffer than the Soleus and Gastrocnemius tendons. The value of the stiff tendon can be discussed in terms of helping the two-muscle-tendon unit combination achieve fine control, without compromising energetics.

In general, muscles with compliant tendons, like series elastic actuators, have low bandwidth and lack of ability to perform fine position control. However, having two muscle-tendon units loading a stiff spring may allow them to act synergistically and achieve finer control over the foot positions, while still benefitting from the catapult effects of their individual series compliances. This can be seen by imagining that even if the two muscle-tendon units move significantly due to their individual tendon compliances, they would have to produce very high forces to overcome the stiff load spring and change foot position significantly, and these high forces may be unlikely in physiological ranges given the neural control and muscle-tendon unit dynamics. This is an especially interesting observation in light of the previously mentioned studies reporting kinematic repeatability of foot motions [3].

Thus the architecture of the Soleus, Gastrocnemius and Achilles tendon units appears to give the combination the best of both worlds - by providing both the fine position control of stiffness and the energetic advantages of compliance. To understand these energetic advantages further, we look at another conserved trend in the optimization results.

Muscle Rest Length to Tendon Slack Length Ratio

Our system ID optimization consistently settled on tendon slack length values that yield repeatable muscle optimum length to tendon slack length ratios - for all muscles and subjects - suggesting that these ratios are conserved. Optimized values agree with

Table 5.3: Muscle Rest Length to Tendon Slack Length Ratios

Subject	**Soleus**			**Gastroc**			**TibAnt**		
	$l_{\mathbf{opt}}$**[cm]**	$l_{\mathbf{sl}}$ **[cm]**	**Ratio**	$l_{\mathbf{opt}}$**[cm]**	$l_{\mathbf{sl}}$ **[cm]**	**Ratio**	$l_{\mathbf{opt}}$**[cm]**	$l_{\mathbf{sl}}$ **[cm]**	**Ratio**
JS	3.62	27.9	0.130	5.44	44.9	0.121	11.8	27.8	0.423
KE	3.27	25.8	0.127	4.91	40.9	0.120	10.6	25.2	0.423
RS	3.42	26.5	0.129	5.14	43.9	0.117	11.1	23.8	0.468
EJ	2.85	21.8	0.130	4.27	34.0	0.128	9.41	22.0	0.428
AS	3.28	25.8	0.127	4.91	41.4	0.119	10.7	21.4	0.503
Average (SD) Ratio	0.129 (0.002)			0.121 (0.004)			0.449 (0.036)		
Delp 1990 Ratio	0.112			0.128			0.454		

a literature report based on cadaver data for l_{opt} and manual tuning of slack lengths based on kinematic and kinetic data. Differences may have arisen from geometric variations like in Section 5.1.1.

The ratios are significant in view of muscle performance. For a given muscle-tendon unit motion and force, muscle active-state and tendon stiffness, the ratio of l_{opt} to l_{sl} determines whether the muscle will operate in isometric, concentric or eccentric contraction. Thus, during a movement, the ratio of l_{opt} to l_{sl} determines the muscle fiber contractile velocity and the muscle metabolic consumption. This feature of the ankle plantar flexor system dynamics has been discussed in [29]. We use our estimates of neurally commanded muscle active state to provide another dimension to this discussion.

5.3.2 Control - Timing Elastic Storage and Release

Another way to look at the $\frac{l_{opt}}{l_{sl}}$ ratio is that it determines the optimum timing of elastic energy storage and release. For a given ratio and the known system dynamics, there is an optimum time in gait cycle when the muscle can start to slowly store energy in the tendon, and a time after which a release in rapid recoil of stored elastic energy would become the most efficient action. We posit that these times are related to the timing and shape of the muscle activation profiles - because muscle activation has to rise above zero when the tendon stretches above slack (MTU dynamics). We see this trend in the solutions to our system model using data-based estimates of muscle activation. This attests to the so-called catapult effect discussed in the literature

- where a mechanism of controlled storage and release of elastic energy results in metabolic energy savings [37].

5.3.3 Structure and Control: Efficiency

Having described the independent effects of structural and control aspects on metabolic savings, we now show the efficiency performance metrics resulting from both these aspects. To illustrate the point that neural-structural interplay is needed for efficient operation, we calculate two efficiencies: (a) one that involves the neural aspect alone and does not account for tendon morphological effects on mechanical work outcomes, and (b) one that involves both neural and tendon effects. We discuss these 'tendon unaccounted' and 'tendon accounted' calculations in order.

Tendon Unaccounted

Our model allows us to calculate efficiency of plantar flexor muscle operation - since we have (a) individual muscle state profiles, (b) individual muscle force profiles and (c) metabolic cost. We accounted for mechanical work and metabolic cost during positive mechanical work phase of muscle operation (i.e. when the muscle is shortening):

$$e_{\text{no tendon}} = \frac{\int F\, dl}{\int a(t) \cdot F_{\max} \cdot v_{\max} \cdot p(v_{\text{CE}}(t))\, dt} \quad \forall dl < 0 \tag{5.4}$$

Table 5.4: Plantar Flexor Muscle Efficiency During Positive Mechanical Work Phases (Tendon Unaccounted)

	Subject	JS	KE	RS	EJ	AS
Train Data	**Metabolic Cost**	9.5	6.8	2.0	4.4	7.1
	Mechanical Work	2.6	1.3	0.43	1.4	1.7
	Muscle Efficiency	0.28	0.19	0.21	0.32	0.25
Test Data	**Metabolic Cost**	11.9	5.7	2.6	5.0	16.0
	Mechanical Work	3.4	1.2	0.55	1.7	3.2
	Muscle Efficiency	0.29	0.20	0.21	0.33	0.20
Test-Train	**Average**	0.28	0.20	0.21	0.32	0.22

Average efficiency for each subject was calculated across test and train data. We see that the average efficiency of muscles doing positive work (across subjects) is 0.25 ± 0.052. This is consistent with empirical measures of performance of skeletal muscle doing positive work [43].

The agreement of numbers, in addition to validating our calculation, shows that the Soleus and Gastrocnemius muscles by themselves are not able to perform at more

than average efficiency. However, this calculation discounts (a) the roles of tendon compliance and (b) the tuning of neural command timings to catapulting effects outlined above.

Tendon Accounted

We did a second efficiency calculation that accounts for both the effects neglected in the previous case.

We calculated the net mechanical work performed by the plantar flexor muscle-tendon units in stance phase (these units perform negligible work in swing). This net mechanical work is equivalent to work at the load (joint in this case):

$$W_{\text{mech}} = \int \tau_{bio}\, d\theta \tag{5.5}$$

The ankle torque and angle for the work calculation were taken from the human gait data, because we did not explicitly model joint angles (only has muscle-tendon state). The model and data mechanical work should be quite close since there is a high agreement between model and data torques, and hence this approximation is valid.

Metabolic work was calculated as:

$$W_{\text{met}} = \sum_i \int \alpha_i(t) \cdot F_{\max,i} \cdot v_{\max,i} \cdot p(v_{\text{CE},i}(t))\, dt \quad \forall t\, \epsilon\, \text{stance} \tag{5.6}$$

In the case of subject RS (starred in table), the Tibialis Anterior was highly active and working hard during mid-stance in addition to plantar flexors, and therefore the TA metabolic cost was included in the sum too.

It is worth mentioning that the metabolic and mechanical calculations above are not restricted to muscle positive work phases, because tendon can be performing positive mechanical work when muscle is working in negative work phase and vice versa.

We defined efficiency as:

$$e_{\text{tot}} = \frac{W_{\text{mech}}}{W_{\text{met}}} \tag{5.7}$$

The calculations are summarized in table 5.5. Across subjects the average efficiency was $0.69 + / - 0.12$. This may be a slight over-estimate since we did not take into account any viscous losses in tendon action. Typically, tendons lose $6 - 15\%$ of their energy to viscous effects. Such losses would cause a decrease in the mechanical work obtained per unit metabolic energy consumed. For a ballpark of the over-estimation, we account a nominal 10% loss in tendon, and recalculate the efficiencies using the numbers in Table 5.5 to arrive at a $0.62 + / - 0.10$ efficiency, or a 7% over-estimation.

Regardless of the tendon losses, the efficiencies in the tendon 'accounted' case are approximately three times higher than the muscle positive work efficiencies from the 'tendon unaccounted' calculation. This shows that the tendon effects are key to high performance. Further, such high gains in efficiency would be unlikely if the neural

Table 5.5: Plantar Flexor Muscle Efficiency (Tendon Accounted)

	Subject	JS	KE	RS	EJ	AS
	Net Mechanical Work	11.6	11.5	10.5	7.8	13.9
Train Data	**Soleus Metabolic Cost**	12.4	5.0	6.2	5.3	6.1
	Gastroc Metabolic Cost	9.0	10.7	7.1	4.1	10.1
	Net Metabolic Cost	21.5	15.7	17.3∗	9.4	16.2
	Mechanical Efficiency	0.54	0.73	0.61	0.83	0.86
Test Data	**Soleus Metabolic Cost**	14.5	4.9	5.3	5.7	5.9
	Gastroc Metabolic Cost	9.9	12.2	4.4	4.3	14.9
	Net Metabolic Cost	24.4	17.1	14.2∗	9.9	20.7
	Mechanical Efficiency	0.48	0.67	0.74	0.79	0.67
Test-Train	**Average**	0.51	0.70	0.67	0.81	0.76

control were not timed for catapult-like action. Thus, the morphological features, the timing of neural commands and muscle dynamics all complement each other to allow for this high metabolic efficiency.

The high plantar flexor efficiencies calculated here are consistent with the 0.61 apparent efficiency obtained empirically in [43][4]. It is worth mentioning that the efficiencies in [43] were 'apparent' estimates since they had to use an exoskeleton, and could not really probe the metabolic cost *in vivo*. Our model adds to their result by calculating these metrics from normal, level ground walking (without any exoskeleton) data and first principles. Further, the analysis in this section highlights the different quantitative features contributing to the large efficiency, and gives us a better understanding of the metabolics of plantar flexor operation.

5.3.4 Section Summary

This section brought together key features of plantar flexor performance arising from (a) tendon morphology, (b) neural control timing and (c) the interplay between the two. For all three cases, we showed model predictions indicating metabolic savings and high efficiency operation in the big, powerful plantar flexor muscles. Our observations are consistent with empirical reports in the literature, and add many new perspectives to these reports.

[4]We can compare our calculation with those in [43] because our calculation of net mechanical work is similar to their exoskeleton work.

5.4 Discussion

This section places the contributions detailed in this chapter in context with the state of the neuromuscular modeling field. Specifically, we discuss differences between our approach and the two classes of inverse approaches to neuromuscular models outlined in Chapter 1.

5.4.1 Dynamic Optimization Studies

First, we discuss comparisons with approaches based on dynamic optimization of neural control [6, 7]:

As introduced in Chapter 1, reference [6] dynamically optimized muscle activations on a full body gait model with set morphological parameters, to minimize a model-based metabolic cost function. Their optimized Soleus and Gastrocnemius activations had peaks close to 1, while the peak active states we estimated from gait EMG data were in the range of $0.4 - 0.5$. Our estimates appear more reasonable as it is strange for the plantar flexors to fully activate in common tasks like level ground self selected speed walking (as opposed to more demanding tasks like running).

We believe that our model captured kinetic trends in the ankle torque with low muscle activity because of our emphasis on the mechanical work benefits of tendon action. When tendon morphology is not identified appropriately, the optimized muscle activities are high, and in turn, the proportional metabolic cost is high too. This is seen in [7] where positive muscle work values are almost two times the numbers expected from empirical estimates in [44]. While we did not model the full leg in this study, we have showed in the previous section that our muscle efficiencies agree with empirical estimates ([43]).

Thus, estimating neural control from data and emphasizing tendon morphology effects gave us more reasonable metrics than dynamically optimizing neural control with set morphology.

5.4.2 Simple Mechanistic Muscle-Tendon Models

Second, we compare the predictive power of our approach with an approach based on simplified, mechanistic representations of muscle-tendon units [8].

This paper represented the Gastrocnemius muscle-tendon unit as a clutch-spring unit. Our length estimates for this muscle predict - from data and first principles - the clutch-like muscle operation of the Gastrocnemius hypothesized in [8]. Further, our modeling effort also provided quantitative insight into the neural control and efficiency metrics that might be driving the isometric operation of this muscle.

The spring in the paper lumps the tendon stiffness as well as the muscle stiffness. Our model decoupled this lumped stiffness into its actively controlled muscle and passive tendon elements. This decoupling allows the model to predict behavior across speed without the parameter modifications that would be necessary with a lumped spring. As a check, we tested a model trained on 1.25 m/s walking data for subject KE, against his 1.50 m/s data. We observed R^2 values of 0.92, showing good agreement

of model torque with the 1.50 m/s empirical ankle torque. This suggests that the neural control actively modulates the muscle stiffness for the higher power needed at greater speeds (consistent with [45]). The emergent property of the optimized tendon parameters is consistent with the parameter invariance resulting from training the model separately on 1.25 m/s and 1.50 m/s data from this subject (Section 4.2.1).

Thus, estimating neural control from data and emphasizing tendon morphology effects gave us (a) quantitative understanding of features driving Gastrocnemius operation, and (b)a preliminary result on emergent adaptability of the model to speed increases in walking.

5.4.3 Section Summary

In summary, our modeling approach adds to the two main categories of inverse neuromuscular models aimed at gaining mechanistic insight into principles governing gait. The key value of this work lies in the ability to decouple muscle and tendon action, and to study impedance modulation resulting from variations in neural control, all while capturing accepted performance metrics such as energetic economy.

5.5 Chapter Summary

This chapter showed that our framework captures many empirical results under an integrated approach derived from first principles. We discussed model predictions about plantar flexor muscle state, tendon structure and energetic performance. Finally, we analyzed these metrics to elucidate some insights regarding structure and control of the ankle plantar flexors with a view to their function and performance in walking. We summarize the key contributions:

1. Plantar flexor length and velocity predictions highlight the role of the Soleus as a steady efficient force generator and that of the Gastrocnemius as a burst mechanical power source. The model captured the differences and similarities in two sets of in vivo measurements for the Gastrocnemius length - showing that subject to subject differences may have led to disparities in empirical measures.

2. We discussed how metabolic savings and increased performance result from (a) long, compliant plantar flexor tendons with conserved slack lengths and (b) catapulting effects arising from controlled storage and release of energy. We demonstrated the high energetic performance of these muscles by evaluating operating efficiencies of 0.69 ± 0.12.

Our results about muscle state, morphological features, in vivo efficiencies and impedance variations showcase the model's potential as a means for obtaining empirically inaccessible measures of the roles of neural control and leg structure in locomotion.

Chapter 6

Conclusions and Future Work

6.1 Conclusions

The thesis set out to develop an inverse computational framework to capture insights about co-operation of neural control and musculo-skeletal structures spanning the ankle joint during walking. It provided arguments to reframe this problem as one of estimating the evolution of individual muscle state during gait.

The key contribution of this thesis is a hybrid mechanistic-statistical approach that (a) explains human gait data, (b) estimates individual ankle muscle state profiles and (c) predicts quantitative metrics consistent with independent empirical studies. The modeling exercise undertaken provided insight into the complementary nature of neural control and leg structure manifest in (a) the roles of individual ankle plantar flexor muscles and (b) the energetic performance of these muscles.

The results demonstrate the viability of our hypothesis that neural control and leg morphology have co-evolved for energetically optimal walking motions. The model predictions underscore the importance of neural-structural interactions in locomotion.

6.2 Scientific Applications

Impedance modulation of muscle is a key feature that captures both intent and feel (feed-forward and feed-back control) as detailed in Chapter 2. The framework described in this thesis gives us access to impedance variations in the ankle muscle-tendon unit (since individual muscle state and dynamics have been estimated). These profiles could be studied to elicit quantitative insights about the roles of neural control circuits, muscle function and leg design in level ground and non-level ground walking.

Ankle Behavior across Speed and Terrain: How do the plantar flexors behave during speed variations in walking? Suggestions about adaptability of the model across speed were made in Chapters 4-5. Are there ways to generalize this to slower speeds in addition to faster speeds? The challenge with slower speeds could stem from the high variability of muscle activation profiles during conscious targeted walking. What is the role of the dorsiflexor during terrain variations in walking? The dorsiflexor

tendon morphology did not have much importance in this optimization as the plantar flexor cost dominated over the dorsiflexor cost. However, if the optimization were to be performed in the nested fashion suggested in Section 4.2.1, with cost including both stance and swing, we may get more insight into dorsiflexor behavior.

Reflexes and Intent: In addition to overall impedance modulation of muscle, modifications of the modeling approach advanced in this thesis could be used with additional empirical data or perturbation studies to elucidate separation of the effects of feed-forward and feedback circuits.

For example, nerve cooling or other agents could be used to block ankle reflex circuits [46] in humans while collecting gait data. Then our modeling framework could predict differences in net active state and joint dynamics arising from blocking specific reflexes. This could shed light on the roles of feed-forward components and/or specific reflexes in muscle and joint dynamics. Interesting questions regarding these feed-forward and feedback components could range from when they are active to how much they influence muscle action.

Another alternative is to apply different perturbations to the joint motion, dynamics and/or muscle state estimates *in silico*, and test classes of reflex circuits (positive force feedback, negative velocity feedback, stretch reflexes or others?) for those that help deal best with the perturbations. Such an approach could help elucidate the kinds of "environmental" variations dealt with by different reflex circuits, and suggest experiments to verify insights. Further it may reveal whether reflex circuits cause adaptation by forcing return to the base strategy, or in some other fashion.

Full Leg Models: Extending this modeling framework to the full leg could potentially capture features such as energy flows between the different elements. Further it could give physical insight into key mechanistic features (force source, strut, brake etc) representing functions of different muscles in walking. Challenges here could be both empirical and analytical.

The model's predictive power is as good as the information content of the data driving it. Surface EMG data for small, deep[1] muscles, or overlapping muscles (example Rectus Femoris and Vasti muscles) is generally low in information content. Particle-filter or other Monte Carlo based techniques as described in Chapter 4 could be attempted to better the accuracy and reliability of active-state estimates obtained from EMG of such muscles. Needle EMG could also help in these cases.

Further, enforcing the torque-constraints as proposed in Chapter 3 may turn out to be difficult for joints that are spanned by a multitude of small muscles (e.g. knee joint). Finally, there may be no easily apparent role divisions for muscles that are not big, well-defined and phasic in activity.

Impedance Matching: It has been shown that the optimal synergistic activation of power-generating muscles interacting with a load corresponds with muscle-load impedance matching [34]. In this thesis, we suggested that neural control comple-

[1]EMG signals are generally better for shorter muscles since they are driven by the nervous system with higher amplitudes and more distinct phasic features

ments the tendinous loading on a muscle for optimal economy of muscle operation during walking. An interesting question is whether this energetic optimality extends to an impedance match between muscle-tendon unit and load.

A simple example where this holds is the actuator-spring-mass system, where the minimum energy consumed by the actuator driving a mass, is at resonance (impedance match) between the spring and mass.

Does the neural control of powerful muscles during walking cause an impedance match between muscle and tendon, or between muscle and tendon + joint load, or groups of muscle-tendon units? Is this the way it ensures maximal power transfer and energy savings? If the match exists, is it instantaneously imposed or as an 'average' feature over time? In other words, are neural control and morphology co-tuned for an impedance match between tendon and muscle during walking (or some other task)? The setup in [34] could be modified to perform some *in vitro* experiments and optimization studies to test this hypothesis.

6.3 Engineering Applications

Insights obtained from our modeling approach could be valuable in the design and control of biologically inspired prosthetic and orthotic devices.

Design: The framework in this thesis offers a rigorous way to derive mechanistic insight into operational modes of different muscles (e.g. the clutch-spring approximation of the Gastrocnemius muscle). This could be valuable in the design of bio-mimetic prostheses and orthoses. Similarly, the tendon compliances obtained and insights on role divisions between muscles could serve useful to a device designer.

Encoding Human-Like Control: Further, the neural control information gained from this approach could inform strategies for controlling these devices. Recently a neuromuscular model-based controller was used to encode a reflexive adaptation to slopes in a powered ankle prosthesis [47]. Neural control information gained from the study in this thesis could be used to encode adaptation to other terrain variations and/or speeds in similar powered ankle prostheses. Similar to work in [47], the state of the prosthesis could be fed into a virtual neuromuscular model based on a height-weight matched intact limbed individual. The model could then compute responses to ground and task variations, and command dynamics that mimic a healthy individual's response.

Myo-electric Control: In addition to encoding adaptation to environmental variations, our framework provides a mechanistic way to interface assistive devices with the wearer's 'intent' (as encoded in EMG signals from the user). Most myo-electric interfaces in the literature are black box models [48, 49]. Our approach, on the other hand, uses the physics of the system to compute individual muscle forces from myo-electric data and joint motion recordings. The preliminary result on speed variations in Chapters 4-5 shows promise for the model's ability to resolve task-based changes in torque resulting from individual muscle impedance modulations. This emergent

adaptability of the model, if seen on tasks other than walking, may add a natural myo-electric interfacing capability to prostheses (as opposed to the more common volitional control).

There, however, is the interesting challenge of understanding (or having an automated controller understand) the differences in EMG data obtained from healthy intact limbed patients (on which the model would be based), and from the amputee or orthotic patient using the device.

EMG data from amputees may be unreliable and activation profiles fed into the model may need to be normalized to amputee stump muscle size. Further, the EMG data fed into the framework described here contains information about feed-forward and feedback contributions to muscle activity. The latter may be lacking in amputees, or at least the feedback going back to the spine in an amputee may depend on different features - such as interactions between the stump and socket. For example, the EMG data from stump muscles could be representative of the instability of the stump on the socket (as amputees tend to fire their muscles a lot to stiffen them and counter the instability). There are possibilities to use good sensors of these interactions to understand this feedback, and inform the use of the framework outlined here in such cases.

Clinical Value: Finally, the framework could help quantitatively evaluate gait pathologies resulting from neurological or musculoskeletal disorders. With modifications tailored toward specific disorders, it could enable an extension of the commonly used clinical electro-myographic measure to the realm of differences in individual muscle dynamics. Having a tool to quantitatively compare impedance modulation/dynamics in patients against the template of a healthy individual could be clinically valuable. Further, the same tool could inform the design/control of assistive devices that can appropriately compensate for specific pathologies to achieve clinical goals.

Appendix A

Muscle-Tendon Parameters

Average adult male muscle parameters from Table 3.3 scaled to subject dimensions using SIMM's scaling algorithm [29]. The scaled parameters for left and right legs

Table 1: Subject-Specific (Scaled) Muscle-Tendon Parameters

Subject	$l_{\mathbf{opt}}$ **[cm]**			$F_{\mathbf{max}}$ **[N]**			$l_{\mathbf{sl}}$ **[cm]**		
	SOL	**MG**	**TA**	**SOL**	**GAS**	**TA**	**SOL**	**MG**	**TA**
JS	3.6	5.4	11.8	5045	1935	723	32.4	49.3	26.8
KE	3.3	4.9	10.6	4554	1746	654	29.2	44.5	24.2
RS	3.4	5.1	11.1	4765	1829	683	30.6	46.6	25.3
EJ	2.8	4.3	9.4	3974	1520	579	25.5	38.7	21.4
AS	3.3	4.9	10.7	4563	1747	661	29.3	44.5	24.5

are averaged to obtain the values fed into the model. As stated in Section 3.5.3, the $F_{\max}$ values of the medial and lateral Gastrocnemius heads are summed to find the $F_{\max}$ of the modeled effective Gastrocnemius. Values listed for muscle isometric forces $F_{\max}$ and tendon slack lengths l_{sl} are the nominal values scaled with optimized factors during system ID (Section 3.5.5, Table 3.4).

Optimization Bounds

For the System Identification, we used the subject specific optimization bounds listed in Table 2. The bounds listed are influenced by the subject specific nominal values

Table 2: Subject-Specific Optimization Bounds

Subject	**JS**		**KE**		**RS**		**EJ**		**AS**	
Parameter	Min	Max	Min	Max	Min	Max	Min	Max	Min	Max
$F_{\mathbf{max,SOL}}$ **[N]**	4036	20180	3643	18214	3812	19060	3179	15896	3650	18251
$F_{\mathbf{max,GAS}}$ **[N]**	1548	7740	1397	6986	1463	7315	1216	6081	1398	6990
$F_{\mathbf{max,TA}}$ **[N]**	579	2895	524	2618	547	2735	463	2317	529	2644
$l_{\mathbf{sl,SOL}}$ **[cm]**	19.7	33.2	17.5	30.1	18.4	31.0	14.9	25.8	17.5	29.3
$l_{\mathbf{sl,GAS}}$ **[cm]**	31.5	51.4	28.2	46.6	29.6	47.9	24.1	40.2	28.2	46.0
$l_{\mathbf{sl,TA}}$ **[cm]**	18.7	29.4	16.9	27.1	17.7	27.4	15.0	23.8	17.1	27.9

in Table 1. The setting of bounds for the optimization is detailed in Section 3.5.5, Table 3.4.

Bibliography

[1] M. Srinivasan and A. Ruina, "Computer optimization of a minimal biped model discovers walking and running," *Nature*, vol. 439, no. 7072, pp. 72–75, 2006.

[2] S. H. Collins, M. Wisse, and A. Ruina, "A Three-Dimensional Passive-Dynamic walking robot with two legs and knees," *The International Journal of Robotics Research*, vol. 20, pp. 607–615, July 2001.

[3] Y. P. Ivanenko, R. Grasso, V. Macellari, and F. Lacquaniti, "Control of foot trajectory in human locomotion: Role of ground contact forces in simulated reduced gravity," *J Neurophysiol*, vol. 87, pp. 3070–3089, June 2002.

[4] F. Mechsner, D. Kerzel, G. Knoblich, and W. Prinz, "Perceptual basis of bimanual coordination," *Nature*, vol. 414, pp. 69–73, Nov. 2001.

[5] I. A. Rybak, K. Stecina, N. A. Shevtsova, and D. A. McCrea, "Modelling spinal circuitry involved in locomotor pattern generation: insights from the effects of afferent stimulation," *The Journal of Physiology*, vol. 577, pp. 641–658, Dec. 2006. PMID: 17008375.

[6] F. C. Anderson and M. G. Pandy, "Dynamic optimization of human walking," *Journal of Biomechanical Engineering*, vol. 123, pp. 381–390, Oct. 2001.

[7] R. R. Neptune, K. Sasaki, and S. A. Kautz, "The effect of walking speed on muscle function and mechanical energetics," *Gait & Posture*, vol. 28, pp. 135–143, July 2008.

[8] K. Endo and H. Herr, "An underactuated model of human walking," *The International Journal of Robotics Research*, vol. *in press*, Nov. 2009.

[9] H. Geyer and H. Herr, "A muscle-reflex model that encodes principles of legged mechanics produces human walking dynamics and muscle activities," *IEEE Transactions of Neural Systems and Rehabilitation Engineering*, vol. *submitted for publication*, Sept. 2009.

[10] J. Perry, *Gait Analysis: Normal and Pathological Function*. New York: Academic Press, third ed., Feb. 1992.

[11] J. Rose and J. G. Gamble, eds., *Human Walking*. Philadelphia: Lippincott Williams & Wilkins, third ed., Sept. 1977.

[12] A. V. Hill, "The heat of shortening and the dynamic constants of muscle," *Royal Society of London Proceedings Series B*, vol. 126, pp. 136–195, Oct. 1938.

[13] A. V. Hill, *First and Last Experiments in Muscle Mechanics*. Cambridge, UK: Cambridge University Press, 1970.

[14] Authors, *Multiple Muscle Systems: Biomechanics and Movement Organization*.

[15] H. Hatze, "A myocybernetic control model of skeletal muscle," *Biological Cybernetics*, vol. 25, no. 2, pp. 103–119, 1977. PMID: 836914.

[16] S. P. Ma and G. I. Zahalak, "A distribution-moment model of energetics in skeletal muscle," *Journal of Biomechanics*, vol. 24, no. 1, pp. 21–35, 1991. PMID: 2026631.

[17] F. E. Zajac, "Muscle and tendon: properties, models, scaling, and application to biomechanics and motor control," *Critical Reviews in Biomedical Engineering*, vol. 17, no. 4, pp. 359–411, 1989. PMID: 2676342.

[18] T. A. McMahon, *Muscles, Reflexes and Locomotion*. Princeton, NJ: Princeton University Press, 1984.

[19] S. L. Delp, J. P. Loan, M. G. Hoy, F. E. Zajac, E. L. Topp, and J. M. Rosen, "An interactive graphics-based model of the lower extremity to study orthopaedic surgical procedures," *IEEE Transactions on Bio-Medical Engineering*, vol. 37, pp. 757–767, Aug. 1990. PMID: 2210784.

[20] R. I. Close, "Dynamic properties of mammalian skeletal muscles," *Physiological Reviews*, vol. 52, no. 1, pp. 129–197, 1972. PMID: 4256989.

[21] N. Hogan, "A review of the methods of processing EMG for use as a proportional control signal," *Biomedical Engineering*, vol. 11, pp. 81–86, Mar. 1976. PMID: 1252567.

[22] N. Hogan and R. W. Mann, "Myoelectric signal processing: Optimal estimation applied to electromyography," *Biomedical Engineering, IEEE Transactions on*, vol. BME-27, no. 7, pp. 382–410, 1980.

[23] T. D. Sanger, "Bayesian filtering of myoelectric signals," *J Neurophysiol*, vol. 97, pp. 1839–1845, Feb. 2007.

[24] E. A. Clancy, E. L. Morin, and R. Merletti, "Sampling, noise-reduction and amplitude estimation issues in surface electromyography," *Journal of Electromyography and Kinesiology*, vol. 12, pp. 1–16, Feb. 2002. PMID: 11804807.

[25] C. S. Taylor, "Isometric muscle contraction and the active state: An analog computer," *Biophysical Journal*, vol. 9, pp. 759–780, June 1969.

[26] A. Hof and J. V. den Berg, "EMG to force processing III: estimation of model parameters for the human triceps surae muscle and assessment of the accuracy by means of a torque plate," *Journal of Biomechanics*, vol. 14, no. 11, pp. 771–777, 779–785, 1981.

[27] G. S. Sawicki and D. P. Ferris, "Powered ankle exoskeletons reveal the metabolic cost of plantar flexor mechanical work during walking with longer steps at constant step frequency," *The Journal of Experimental Biology*, vol. 212, no. Pt 1, pp. 21–31, 2009. PMID: 19088207.

[28] C. Winby, D. Lloyd, and T. Kirk, "Evaluation of different analytical methods for subject-specific scaling of musculotendon parameters," *Journal of Biomechanics*, vol. 41, no. 8, pp. 1682–1688.

[29] S. L. Delp, *Surgery simulation: A computer graphics system to analyze and design musculoskeletal reconstructions of the lower limb*. PhD thesis, Stanford University, 1990.

[30] R. C. Woledge, N. A. Curtin, and E. Homsher, *Energetic Aspects of Muscle Contraction*. Academic Press, May 1985.

[31] Z. Michalewicz, "A survey of constraint handling techniques in evolutionary computation methods," *Proceedings of the 4th Annual Conference on Evolutionary Programming*, pp. 135—155, 1995.

[32] O. Yeniay, "Penalty function methods for constrained optimization with genetic algorithms," *Mathematical and Computational Applications*, vol. 10, pp. 45—56, 2005.

[33] K. Deb, "An efficient constraint handling method for genetic algorithms," *Computer Methods in Applied Mechanics and Engineering*, vol. 186, pp. 311—338, 1998.

[34] W. Farahat, *Optimal Workloop Energetics of Muscle-Actuated Systems*. PhD thesis, Massachusetts Institute of Technology, 2007.

[35] T. D. Johnson, R. M. Elashoff, and S. J. Harkema, "A bayesian change-point analysis of electromyographic data: detecting muscle activation patterns and associated applications," *Biostatistics*, vol. 4, pp. 143–164, 2003.

[36] G. J. van Ingen Schenau, "An alternative view of the concept of utilisation of elastic energy in human movement," *Human Movement Science*, vol. 3, pp. 301–336, Dec. 1984.

[37] M. Ishikawa, P. V. Komi, M. J. Grey, V. Lepola, and G. Bruggemann, "Muscle-tendon interaction and elastic energy usage in human walking," *J Appl Physiol*, vol. 99, pp. 603–608, Aug. 2005.

[38] G. Lichtwark, K. Bougoulias, and A. Wilson, "Muscle fascicle and series elastic element length changes along the length of the human gastrocnemius during walking and running," *Journal of Biomechanics*, vol. 40, no. 1, pp. 157–164.

[39] T. Fukunaga, K. Kubo, Y. Kawakami, S. Fukashiro, H. Kanehisa, and C. N. Maganaris, "In vivo behaviour of human muscle tendon during walking.," *Proceedings of the Royal Society B: Biological Sciences*, vol. 268, no. 1464, p. 229, 2001.

[40] A. V. Hill, "The efficiency of mechanical power development during muscular shortening and its relation to load," *Proceedings of the Royal Society of London. Series B, Biological Sciences*, vol. 159, no. 975, 1964.

[41] S. W. Trappe, T. A. Trappe, G. A. Lee, and D. L. Costill, "Calf muscle strength in humans," *International Journal of Sports Medicine*, vol. 22, pp. 186–191, Apr. 2001. PMID: 11354521.

[42] G. A. Lichtwark and A. M. Wilson, "Optimal muscle fascicle length and tendon stiffness for maximising gastrocnemius efficiency during human walking and running," *Journal of Theoretical Biology*, vol. 252, pp. 662–673, June 2008. PMID: 18374362.

[43] G. S. Sawicki and D. P. Ferris, "Mechanics and energetics of level walking with powered ankle exoskeletons," *J Exp Biol*, vol. 211, pp. 1402–1413, May 2008.

[44] J. M. Donelan, R. Kram, and A. D. Kuo, "Mechanical work for step-to-step transitions is a major determinant of the metabolic cost of human walking," *J Exp Biol*, vol. 205, pp. 3717–3727, Dec. 2002.

[45] D. A. Winter, "Biomechanical motor patterns in normal walking," *Journal of Motor Behavior*, vol. 15, pp. 302–330, Dec. 1983. PMID: 15151864.

[46] M. J. Grey, M. Ladouceur, J. B. Andersen, J. B. Nielsen, and T. Sinkjaer, "Group II muscle afferents probably contribute to the medium latency soleus stretch reflex during walking in humans," *The Journal of Physiology*, vol. 534, pp. 925–933, Aug. 2001. PMID: 11483721.

[47] M. Eilenberg and H. Herr, "Control of a powered ankle-foot prosthesis based on a neuromuscular model," *IEEE Transactions of Neural Systems and Rehabilitation Engineering*, vol. *accepted for publication*, Aug. 2009.

[48] L. Wang and T. Buchanan, "Prediction of joint moments using a neural network model of muscle activations from EMG signals," *IEEE Transactions on Neural Systems and Rehabilitation Engineering*, vol. 10, no. 1, pp. 30–37, 2002.

[49] E. E. Cavallaro, J. Rosen, J. C. Perry, and S. Burns, "Real-time myoprocessors for a neural controlled powered exoskeleton arm," *IEEE Transactions on Biomedical Engineering*, vol. 53, no. 11, pp. 2387–2396, 2006.